Revision 3 Word Count: 11570

Quartz texture and chemical composition fingerprint ore-forming fluid evolution at Bilihe porphyry Au deposit, NE China

Jingxin Hong[1, 2], Degao Zhai[1*], Manuel Keith[2]

[1]*State Key Laboratory of Geological Processes and Mineral Resources, and School of Earth Sciences and Resources, China University of Geosciences, Beijing 100083, China*

[2]*GeoZentrum Nordbayern, Friedrich-Alexander-Universität Erlangen-Nürnberg, Erlangen 91054, Germany*

[*]*E-mail: dgzhai@cugb.edu.cn*

Revised submission to: ***American Mineralogist***

With 11 Figures, 1 Table, and 4 Supplemental Tables

24-Aug-2023

ABSTRACT

Quartz is widely distributed in various magmatic-hydrothermal systems and shows variable textures and trace element contents in response to multiple generations, enabling this mineral phase to serve as a robust tracer for monitoring hydrothermal fluid evolution. This study highlights that integrated high-resolution SEM-CL textures and trace element data of quartz can be used to constrain physicochemical fluid conditions and trace the genesis of quartz in porphyry ore-forming systems. The Bilihe deposit is a Au-only porphyry deposit located in the Central Asian orogenic belt, NE China. Four quartz generations were distinguished following a temporal sequence from early-stage dendritic quartz, unidirectional solidification textured quartz (UST quartz), gray banded vein quartz (BQ), to late-stage white calcite vein quartz (CQ), with the Au precipitation being mostly related to dendritic quartz, UST quartz, and BQ. The well-preserved dendritic quartz with sector-zoned CL intensities and euhedral oscillatory growth zones crystallized rapidly during the late magmatic stage. The relatively low Al contents of dendritic quartz were interpreted to be related to accompanied feldspar or mica crystallization, while the high Ti contents indicate high crystallization temperatures (~750 °C). The comb-layered UST quartz displays heterogeneous patchy luminescence with weak zoning, hosts coeval melt and fluid inclusions, and retains the chemical characteristics of magmatic dendritic quartz. High Ti and low Al contents of UST quartz suggest a formation at relatively high temperatures (~700 °C) and high pH conditions. Three sub-types can be defined for

hydrothermal BQ (BQ1, BQ2, and BQ3) based on contrasting CL features and trace element contents. The Al contents increase from BQ1 to BQ2 followed by a drop in BQ3, corresponding to an initial decrease and subsequent increase in fluid acidity. Temperature estimates of BQ decrease from BQ1 (635 °C) to BQ3 (575 °C), which may, however, be disturbed by high growth rates and/or high TiO_2 activity. The CQ typically displays a CL-bright core and CL-dark rim with oscillating CL intensities, and is characterized by the lowest Ti and highest Al, Li, and Sb contents compared to the other quartz types, which suggests a deposition from more acidic and lower temperature fluids (~250 °C). Trace element patterns indicate that a coupled $Si^{4+} \leftrightarrow (Al^{3+}) + (K^{+})$ element exchange vector is applied for dendritic quartz, UST quartz, and BQ. By contrast, charge-compensated cation substitution of $Si^{4+} \leftrightarrow (Al^{3+}, Sb^{3+}) + (Li^{+}, Rb^{+})$ is favored for CQ. The comparison with compiled trace element data of quartz from other porphyry Au, Cu, and Mo deposits worldwide suggests that Ti, Al, Li, K, and Ge concentrations, as well as Al/Ti and Ge/Ti ratios, have the potential to discriminate metal fertility of porphyry mineralization.

Keywords: Bilihe; porphyry Au deposit; quartz; SEM-CL texture; trace elements; fluid evolution

INTRODUCTION

Quartz is one of the most ubiquitous gangue minerals in veins and veinlets of

magmatic-hydrothermal ore deposits. In porphyry-type deposits, stockwork veins commonly constitute multiple quartz generations, which are characterized by typical dissolution and juxtaposition textures (e.g., Rusk and Reed 2002; Bennett 2014; Pan et al. 2019). However, accurately recognizing the internal textures or temporal relationships of quartz via naked eyes or traditional petrographic techniques is difficult (e.g., Götze et al. 2004; Frelinger et al. 2015; Qiu et al. 2021). Scanning electron microscope cathodoluminescence (SEM-CL) is an effective tool to reveal the defect structure of minerals, enable the visualization of the homogeneity or heterogeneity of quartz crystals, distinguish different quartz generations, and deconvolute the sequence of mineralizing events (e.g., Rusk and Reed 2002; Götze et al. 2004, 2012, 2021; Rusk et al. 2008; Maydagán et al. 2015). Additionally, trace element analysis by laser ablation-inductively coupled plasma-mass spectrometry (LA-ICP-MS) can provide important information about trace element concentration and incorporation in different quartz generations (e.g., Tanner et al. 2013; Maydagán et al. 2015; Breiter et al. 2017; Mao et al. 2017). Accordingly, the combination of SEM-CL and LA-ICP-MS analysis is instructive for constraining various physicochemical fluid parameters, such as temperature, pressure, pH, and initial melt/fluid composition, as well as tracking fluid pathways, fluid-rock reactions, fluid evolution, and mineral precipitation in magmatic-hydrothermal systems (Rusk and Reed 2002; Götze et al. 2004; Rusk et al. 2008; Müller et al. 2010; Tanner et al. 2013; Maydagán et al. 2015; Breiter et al. 2017; Gao et al. 2022; Raimbourg et al. 2022). Most

81 studies devoted to CL textures and trace element chemistry of quartz in porphyry deposits
82 have focused on the common Cu/Mo sub-types (e.g., Redmond et al. 2004; Landtwing
83 and Pettke 2005; Rusk et al. 2006, 2008; Rusk 2012; Müller et al. 2010; Tanner et al.
84 2013; Maydagán et al. 2015; Mao et al. 2017; Rottier and Casanova 2020; Gao et al.
85 2022). However, Au-only porphyry deposits are rarely developed globally (e.g., Sillitoe
86 2010; Yang and Cooke 2019), and as such the processes that lead to variations in the
87 texture and trace element composition of quartz in Au-only porphyries are less well
88 understood (Yang et al. 2015; Huang et al. 2021; Qiao et al. 2022).

89 The Bilihe porphyry Au-only deposit in NE China is such an example, where
90 multiple quartz generations are developed that are closely associated with the Au
91 deposition. Yang et al. (2015) proposed that most of the Au mineralization at Bilihe is of
92 magmatic origin, as supported by petrographic observations on dendritic and
93 comb-layered quartz. Huang et al. (2020) proposed that the unidirectional solidification
94 textured quartz (UST quartz) represents the most fertile unit of Au deposition. Qiao et al.
95 (2022) combined textural observations with fluid inclusions and in-situ oxygen isotope
96 analysis of UST and gray banded vein quartz to investigate the ore-forming conditions of
97 two distinct Au precipitation events. However, the dynamics and kinetics of the complex
98 growth histories of quartz in a relative chronological order are still poorly understood, but
99 provide important new insights to better constrain the Au deposition processes in the
100 Bilihe Au-only porphyry and similar deposits worldwide.

To address the above issues, we performed systematic SEM-CL measurements followed by in-situ trace element analysis of the different quartz generations, as revealed by distinct CL intensities in quartz from the magmatic to hydrothermal stages at Bilihe. On this basis, we constrained the physiochemical conditions and evolutionary history of the mineralizing fluids that controlled the Au deposition.

REGIONAL GEOLOGY

The Central Asian orogenic belt (CAOB) is a Phanerozoic accretionary orogen located between the Siberian and North China Craton (NCC) (Fig. 1a). The belt consists of four main blocks (Fig.1b), including the Erguna, the Xing'an-Airgin Su, the Songliao-Hunshandake, and the Jiamusi blocks, among which the first three are commonly referred as the Xing'an-Mongolian orogenic belt (XMOB; Xu et al. 2014, 2015). These four blocks are separated by four NE-trending sutures, namely the Xinlin-Xiguitu, the Xilinhot-Heihe, the Mudanjian, and the Ondor Sum-Yongji sutures (Fig. 1b; Xu et al. 2014, 2015). Tectonically, the Bilihe porphyry Au-only deposit is hosted by the EW-trending middle Ordovician to early Silurian Bainaimiao arc (Yang et al. 2016), which is located along the northern margin of the NCC and to the south of the Solonker suture zone (Fig. 1c). It is debated whether the Bainaimiao arc was an island arc (Zhang et al. 2014) or a subduction-related continental margin arc (Xiao et al. 2003; Yang et al. 2016). The arc consists of early Paleozoic calc-alkaline volcanic sequences of

basaltic, andesitic, and rhyolitic lavas; and an intrusive complex of quartz diorite, tonalite, and minor gabbro, granodiorite, and granite (Tang and Yan 1993; Nie and Bjørlykke 1999; Yang et al. 2016).

The northern margin of the NCC records a complicated series of geodynamic events (e.g., Xiao et al. 2003; Zhang et al. 2010; Wu et al. 2011; Xu B et al. 2013; Xu W et al. 2013; Wilde 2015), with the formation of numerous different types of ore deposits during subsequent stages of tectonic evolution in the region (Zhao et al. 2021a, 2023; Hong et al. 2021; Zhai et al. 2019, 2020). Widespread Permian intrusive rocks include monzonite, granite porphyry, granodiorite (280 Ma; Zhang et al. 2020), biotite adamellite (274-268 Ma; Xiao et al. 2012), and minor gabbro (279 Ma; Liu et al. 2019). Most of them relate to the I-type series with subordinate A-type intrusions, resulting from the southward subduction of the Paleo-Asian oceanic plate underneath the northern margin of the NCC (e.g., Wu et al. 2011; Liu et al. 2013, 2019; Yang et al. 2016; Zhao et al. 2021b). Available geochronological data show that the porphyry Cu-Au deposits and lode Au deposits hosted in or close to the Bainaimiao arc mainly formed during the late Paleozoic (Fig. 1c), which includes the Bilihe porphyry Au-only deposit (ca. 269 Ma, Zhu et al. 2018) and the Hadamiao Cu-Au deposit (270-266 Ma, Wang et al. 2019). These similar ages reveal that within the constraints of the current geochronology, the ages of Au ore formation and spatially related magmatic activity overlap.

ORE DEPOSIT GEOLOGY

Outcrops in the Bilihe ore district are mainly composed of Permian volcano-sedimentary sequences of basalt, basaltic andesite, rhyolite, and tuff interbedded with minor tuffaceous sandstone, which are covered by Tertiary red mudstone and Quaternary sediments. The mafic to felsic volcanic rocks are of Permian age (andesitic rocks, 281 ± 4 Ma, Qing et al. 2012; rhyolite, 274 ± 3 Ma, Yang et al. 2016) are exposed along an east-northeast trending belt bound by regional faults (Fig. 2a). The faults are predominantly NW-striking and subordinately NE-striking within the ore district (Ge et al. 2009).

The Au ores of the Bilihe deposit are subdivided into the Center I and II orebodies (Fig. 2a). The Center I orebody is dominated by quartz vein-type mineralization and the deposit contains an ore resource of 3.1 t of Au at 6.2 g/t Au, which is associated with a narrow NW-trending quartz diorite dike (Ge et al. 2009). The Center II orebody is located ~1 km to the SW of the Center I orebody (Fig. 2b), and is covered by pre-ore rock units of early Permian andesite, tuff, and Cenozoic sedimentary rocks (Liu and Nie 2015). It is spatially and temporally related to a buried and elongated tongue-shaped intrusion, possibly referring to multiple intrusive events with geochemical compositions varying from diorite in the lower part to granite in the upper part (Yang et al. 2016; Zhu et al. 2018). The Center II orebody is characterized by porphyry-type mineralization and contains >25 t of Au at an average grade of 2.7 g/t Au (Huang et al. 2020). No other ore

161 metals (such as Cu, Mo, Ag) were found in economic grades (Ge et al. 2009). The
162 high-grade (>3 g/t) Au ores are dominantly hosted in the granodiorite porphyry (Fig. 2b),
163 where numerous dendritic quartz phenocrysts and auriferous quartz veins occur (Yang et
164 al. 2015). The granodiorite porphyry shows metaluminous high-K calc-alkaline
165 characteristics at 62.2 to 64.4 wt% SiO_2 (Wang et al. 2019).

166 Hydrothermal alteration zones are well developed in the Center II orebody. From
167 deep to shallow level, the alteration dominantly followed a sequence of potassic
168 (K-feldspar + biotite), phyllic (sericite + quartz + pyrite), intermediate argillic (illite +
169 smectite + carbonate + tourmaline), and propylitic (chlorite + epidote) alteration,
170 superimposed by later carbonatization and silicification (quartz + carbonate ± pyrite ±
171 fluorite) zones (e.g., Li et al. 2021). Pervasive yellow-green intermediate argillic and
172 propylitic alteration have intensely overprinted the early potassic alteration, which is only
173 partly preserved in deeper levels of the porphyry system (Zhu et al. 2018). Tourmaline
174 alteration is widely developed in and surrounding the intrusion, which extends for some
175 meters in the adjacent wall rocks (Li et al. 2021). As a sulfide-poor deposit, the sulfide
176 and sulfosalt minerals at Bilihe have a low modal abundance of <2 vol.% and show a
177 simple mineralogical composition, predominantly including pyrite, chalcopyrite, and
178 molybdenite, with minor pyrrhotite, and tetrahedrite-tennantite. Oxides are mainly
179 composed of magnetite, ilmenite, and minor rutile, which account for ~5 vol% (Yang et
180 al. 2015). As the main Au-hosting mineral, quartz is the most important gangue mineral in

the Bilihe Au-only porphyry deposit. Mineral thermobarometers indicate magma ascent or decompression (from ~ 3-5 kbar to ~ 0.5-1.8 kbar) from a deeper reservoir (~6.5 km) to the final emplacement depth (~2 km) associated with the ore formation (Huang et al. 2020). Fluid inclusions yielded variable pressure estimates ranging from 0.08 to 0.30 kbar for the auriferous quartz veins, suggesting a vein formation at transitional lithostatic to hydrostatic pressure conditions (Qiao et al. 2022).

SAMPLES AND ANALYTICAL METHODS

The quartz-bearing porphyry vein samples were collected from the open pit and from drill cores of the Center II orebody at Bilihe. Polished thin sections were used for petrographic observations and textural classification of quartz and associated minerals in preparation for electron microscopy.

Scanning electron microscope cathodoluminescence (SEM-CL)

The SEM-CL imaging of quartz was carried out using a Tescan thermal field emission SEM equipped with a MIRA3-XMU CL spectrometer at the Research Center of Genetic Mineralogy, China University of Geosciences Beijing (CUGB). An acceleration voltage of 10 kV and beam-current of 10 nA were used. Due to the small field of view, some images presented here are mosaics of multiple CL images digitally stitched together after acquisition. Processing of the SEM-CL images included brightness, contrast, and coloring to facilitate the textural classification of quartz, which was performed by the

ImageJ software (Schneider et al. 2012). The combination of SEM-CL imaging and optical transmitted light microscopy allowed to distinguish quartz textures and generations, which guided the following LA-ICP-MS study and helped to avoid accidental ablation of fluid and mineral inclusions in quartz.

Laser ablation-inductively coupled plasma-mass spectrometry (LA-ICP-MS)

The quantitative trace element composition of the different quartz textures and generations was determined by LA-ICP-MS at the State Key Laboratory of Geological Processes and Mineral Resources at CUGB, using a New Wave UP193SS laser ablation system coupled with an Agilent 7500a ICP-MS. A 36 μm spot size was used with a laser energy density of 10 J/cm^2 and a repetition rate of 10Hz. These conditions led to controlled and continuous ablation of quartz, with only little spalling or fracturing. Helium was used as the carrier gas and argon was used as the make-up gas, which were mixed via a T-connector before entering the torch. The ICP-MS operated in P/A mode with an Ar flow rate of 1 L/min. Oxide production was monitored leading to $^{238}U^{16}O/^{238}U$ values that were consistently <0.6%. For the trace element calibration, NIST SRM610 was used for the external standardization, which was analyzed twice every 10 quartz analyses to monitor the instrument drift. Fifty seconds of background (i.e., gas blank) signal and 55 s of quartz ablation were collected for each analysis. The following elements were measured by LA-ICP-MS: ^{7}Li, ^{9}Be, ^{11}B, ^{24}Mg, ^{27}Al, ^{29}Si, ^{31}P, ^{39}K, ^{44}Ca, ^{45}Sc, ^{49}Ti, ^{55}Mn, ^{57}Fe, ^{65}Cu, ^{66}Zn, ^{72}Ge, ^{85}Rb, ^{88}Sr, ^{90}Zr, ^{93}Nb, ^{98}Mo, ^{107}Ag, ^{121}Sb, ^{133}Cs,

221 ^{137}Ba, ^{139}La, ^{140}Ce, ^{141}Pr, ^{146}Nd, ^{147}Sm, ^{153}Eu, ^{157}Gd, ^{159}Tb, ^{163}Dy, ^{165}Ho, ^{166}Er, ^{169}Tm,
222 ^{172}Yb, ^{175}Lu, ^{182}W, ^{197}Au. Data were processed by GLITTER 4.4.1 using ^{29}Si as the
223 internal standard assuming a stoichiometric quartz composition (Wiedenbeck et al. 1995).
224 The relative standard deviation (RSD) of replicate analyses of NIST SRM610 was <5%
225 for Ti and <10% for all other measured elements (Zhang et al. 2019).

226 # RESULTS

227 ## Quartz petrography and gold occurrence

228 The quartz textures and generations in the Bilihe deposit can be related to three
229 distinct stages: (1) magmatic stage, (2) magmatic to hydrothermal transitional stage, and
230 (3) hydrothermal stage. Dendritic quartz is considered to form in the late magmatic stage,
231 which characteristically has a relatively large size (<0.2 to 5 cm long) and well-preserved
232 arms, suggesting magma undercooling and relatively rapid crystallization (Figs. 3a-b). In
233 the magmatic-hydrothermal transitional stage, unidirectional solidification textured
234 quartz (UST quartz) layers developed (Figs. 3c-d). The thickness of the UST quartz layers
235 ranges from several millimeters to centimeters (Figs. 3c-d, g), and they locally extend for
236 several meters laterally. The crystallization direction of the prismatic UST quartz is
237 consistently inward towards the center of the granitic stocks (Fig. 3c; Erdenebayar et al.
238 2014). Based on crosscutting relations and mineral assemblages, three distinct vein-types
239 in the hydrothermal stage have been recognized in the Bilihe deposit (Figs. 3e-h). The
240 early K-feldspar veins typically represent the earliest hydrothermal event and are crosscut

This is the peer-reviewed, final accepted version for American Mineralogist, published by the Mineralogical Society of America.
The published version is subject to change. Cite as Authors (Year) Title. American Mineralogist, in press.
DOI: https://doi.org/10.2138/am-2022-8840. http://www.minsocam.org/

by later gray banded vein quartz (BQ, Fig. 3e) that show a translucent to gray-black appearance (Figs. 3e-h). The BQ has a thickness of several millimeters and are irregular, discontinuous, and locally accompanied by K-feldspar alteration halos. As such, these veins are potentially analogues to A- and B-type veins known from porphyry Cu deposits (Sillitoe 2010), but lack the common sulfide mineralization at Bilihe. Some of them reopened and were infilled by calcite along the center of the vein or intersected by later calcite veins (Fig. 3h). The late hydrothermal calcite vein quartz (CQ) is white, reaches several centimeters in thickness (Fig. 3h) and consists of carbonate (calcite + dolomite), quartz, pyrite, and tourmaline.

The main Au-bearing quartz units at Bilihe include the dendritic quartz, UST quartz, and BQ (Fig. 4). Gold locally forms clusters or isolated grains (Figs. 4a-b, h-i), commonly as rounded droplets or hexagonal shapes. In the dendritic quartz, Au trails forming straight lines of typically 100 to 500 μm length (Fig. 4b) and locally up to 2,000 μm were observed, which generally lack any spatial relation to fractures (Fig. 4b). By contrast, Au grains of irregular or angular shape either occur in healed micro-fractures that intersect the UST quartz and BQ (Figs. 4c-d, f-g), or coexist with minor sulfides and sulfosalts, such as pyrite, chalcopyrite, and tennantite-tetrahedrite (Figs. 4j-k). Rare amounts of Au are also found in the adjacent alteration zones (Figs. 4g-l).

SEM-CL textures of quartz

This is the peer-reviewed, final accepted version for American Mineralogist, published by the Mineralogical Society of America.
The published version is subject to change. Cite as Authors (Year) Title. American Mineralogist, in press.
DOI: https://doi.org/10.2138/am-2022-8840. http://www.minsocam.org/

The CL images of dendritic quartz revealed sector-zoned features with euhedral concentric growth zoning (Figs. 5a-b). The growth zones are typically 5 to 100 μm in width and parallel to the grain boundary, consisting of micron-scale CL-dark and CL-bright alternating bands. Locally, Au trails hosted in dendritic quartz are consistent with the kink point of concentric CL zones in the host quartz (Fig. 5c; Yang et al. 2015). The growth fabrics in UST quartz are more heterogenous with weak zoning and patchy luminescence (Figs. 5d-e). Some UST quartz grains display CL-bright cores and CL-dark rims (Fig. 5f). Gold grains can be found interstitial between UST quartz crystals (Fig. 5f). Commonly, BQ growth commenced from the vein wall towards the center. Three BQ sub-types (BQ1, BQ2, BQ3) can be distinguished based on their contrasting CL character (Figs. 5g-h). The CL texture of BQ1 is dominated by mosaic or roughly equigranular CL-gray quartz, showing a homogeneous CL intensity. The BQ2 is dominated by euhedrally zoned quartz with micron-scale growth zones of oscillating CL intensity, with local dissolution fronts (Figs. 5g-i). The BQ3 formed interstitial between BQ1 and BQ2 with dissolution textures at the contact boundaries and displays darker CL intensities compared to the two earlier BQ types (Figs. 5g-h). The BQ1 and BQ3 quartz grains usually lack internal growth zones or other internal variations in CL intensity and are intensely fractured by splatter and cobweb textures. Abundant CL-dark magnetite is hosted in BQ1 and BQ2 (Figs. 5g-h). Gold associated with pyrite was observed in fractures of BQ2 (Fig. 5i). The CQ has a euhedral shape with a CL-bright core and

CL-dark growth zones towards the rim (Figs. 5j-k). In some grains, the CL-bright core appears to have embayed edges against the overgrown rim. Splatter and cobweb textures also occur in the CQ grains.

Trace element concentrations

A total of 140 trace element analyses were obtained from the different quartz types, including 40 analyses of dendritic quartz, 30 analyses of UST quartz, 60 analyses of BQ, and 10 analyses of CQ. The analytical results are summarized in Table 1, and the entire dataset is available in Supplemental Table S1. The different trace elements were categorized based on their preferred occupation in the quartz atomic lattice (Larsen et al. 2004; Rottier and Casanova 2020). The reported compositional differences between the different quartz-types generally refer to the median value in the following.

Aluminum, Fe, B, As, Sb, and Ga dominantly form trivalent cations in quartz (Rottier and Casanova 2020). Aluminum and Sb are comparable in most quartz-types except for CQ, which shows the highest contents in these elements (Figs. 6a-b). By contrast, Fe contents in CQ and BQ2 are similar and higher than in the other quartz-types (Fig. 6c). Boron shows a decrease from the magmatic (dendritic quartz) and magmatic-hydrothermal transitional (UST quartz) to the hydrothermal stages (BQ and CQ) (Fig. 6d). Lithium, Na, K, Rb, Cs, and Cu are the main monovalent cations in quartz (Rottier and Casanova 2020). Lithium shows a similar relative variation as Al and Sb (Fig.

301 6e), whereas all other elements of this group do not show systematic variation from
302 dendritic quartz to CQ (Table 1).

303 Titanium and Ge are the main tetravalent cations in quartz (Rottier and Casanova
304 2020). Titanium concentrations decrease slightly from the magmatic (dendritic quartz)
305 and magmatic-hydrothermal transitional stage (UST quartz) to hydrothermal BQ
306 following a significant drop to late-stage CQ (Fig. 6f). Germanium concentrations in
307 quartz show relatively uniform results between 2-10 ppm (Fig. 6g). Magnesium and Mn
308 are the main divalent cations in quartz (Rottier and Casanova 2020). A wide variation
309 between the different quartz-types exceeding two orders of magnitude was observed for
310 Mg, with higher median Mg contents in hydrothermal (BQ and CQ) than in magmatic
311 (dendritic quartz) and magmatic-hydrothermal transitional stage quartz (UST quartz) (Fig.
312 6h, Table 1). Manganese contents slightly increase from dendritic quartz to CQ with
313 respect to the median values (Fig. 6i, Table 1).

314 Chondrite-normalized REE patterns (Sun and McDonough 1989) for most
315 quartz-types are relatively flat (Fig. 7), except for a pronounced La enrichment and
316 negative Eu anomaly (δEu=0.33-1.01). In addition, positive Nd anomalies were observed
317 in some analyses of dendritic quartz, UST quartz, and BQ. The overall compositional
318 REE range of dendritic and UST quartz is relatively uniform, whereas pronounced REE
319 variations were observed between different measurements of BQ and CQ.

320 Two representative grains of (magmatic) dendritic quartz and CQ were selected to

investigate potential trace element variations within single grains with respect to changes in CL intensity (Fig. 8). The CL intensity of dendritic quartz correlates with the Ti, Al, and Ca contents, while the CL intensity of hydrothermal CQ only varies with respect to Ti. In addition, Al and K concentration profiles show a similar relative pattern in dendritic quartz and CQ, but without any relation of the K contents to the CL intensities (Fig. 8).

DISCUSSION

Variations in SEM-CL intensities and implications for quartz chemistry

The physical (e.g., CL intensity and color, micro-inclusion inventory) and chemical (e.g., trace element and isotopic composition) properties of quartz are mostly controlled by the P-T-X conditions during its formation (e.g., Larsen et al. 2004; Götze 2009; Rusk et al. 2011; Rusk 2012; Frelinger et al. 2015; Li et al. 2020; Rottier and Casanova 2020; Götze et al. 2021). Generally, dendritic quartz is thought to be the product of rapid crystallization from highly fractionated magmas during the late magmatic stage (Swanson and Fenn 1986; Yang et al. 2015). For magmatic quartz crystals, CL textures can provide additional information on the P-T-X conditions of the related granitic melts (Götze et al. 2021). The pronounced growth zoning of dendritic quartz (Figs. 5a-b) reflects its magmatic origin and fluctuations in magma temperature, pressure, and melt/fluid composition during crystallization (Erdenebayar et al. 2014; Peng et al. 2010; Li et al. 2011). Quartz and melt/fluid disequilibrium likely led to the destabilization of the quartz

341 growth boundary and changed the intrinsic textures and trace element distribution in
342 dendritic quartz, as preserved by the growth zoning (Peng et al. 2010; Li et al. 2011). The
343 elongated habit of dendritic quartz (Fig. 3b) is controlled by the two- or three-times faster
344 growth rate of quartz along the c-axis compared to the a-axis (Swanson and Fenn 1986).
345 The representative CL image of the sector-zoned texture represents the r and z faces of
346 quartz (Fig. 8a; Yang et al. 2015). The r face commonly shows higher CL intensity and
347 trace element concentrations than the z face (Fig. 8a), implying a faster growth rate for
348 the r face (Swanson and Fenn, 1986; Yang et al. 2015). The relatively low Al
349 concentration in magmatic dendritic quartz compared to the other quartz-types (except
350 BQ3, Fig. 6a) is likely the result of Al consumption by the earlier onset of feldspar and
351 possibly some mica crystallization from the magma (Larsen et al. 2004). Huang and
352 Audétat (2012) showed experimentally that Ti is preferentially incorporated into quartz at
353 higher growth rates. Hence, the high Ti contents in dendritic quartz could be the result of
354 enhanced Ti incorporation in crystal defects during rapid non-equilibrium quartz growth,
355 which could be triggered by degassing during magma ascent (Cernuschi et al. 2018). In
356 addition, it has been shown that the Ti content in quartz positively correlates with its
357 formation temperature in porphyry systems and is decoupled from most other trace
358 elements (Landtwing and Pettke 2005; Rusk et al. 2006; Thomas et al. 2010; Huang and
359 Audétat 2012; Maydagán et al. 2015). Accordingly, the crystallization temperatures of the
360 different quartz-types from Bilihe were estimated by Ti-in-quartz geothermometry

This is the peer-reviewed, final accepted version for American Mineralogist, published by the Mineralogical Society of America.
The published version is subject to change. Cite as Authors (Year) Title. American Mineralogist, in press.
DOI: https://doi.org/10.2138/am-2022-8840. http://www.minsocam.org/

(TitaniQ) following the equation by Huang and Audétat (2012) (Supplemental Table S2). Dendritic quartz yielded unrealistically high crystallization temperatures >900 ℃, which we refer to the non-equilibrium incorporation of Ti in dendritic quartz due to its high growth rates. As a consequence, the lowest Ti contents of dendritic quartz were used, which provide the best approximation of the actual crystallization temperature (~750 °C; Cernuschi et al. 2018).

The comb-layered UST quartz is typically developed in the mineralized granodiorite porphyry at Bilihe, which crystallized during the magmatic-hydrothermal transition at the roof of the magma chamber, where the exsolved aqueous fluids ponded (Lowenstern and Sinclair 1996; Yang et al. 2008; Erdenebayar et al. 2014; Hong et al. 2019; Bain et al. 2022). The zoning patterns of UST quartz (Figs. 5d-e) demonstrate periodic degassing during melt-fluid cooling at the top of the granodiorite porphyry (Erdenebayar et al. 2014). The corrosion along the UST quartz rim (Fig. 5f) may be caused by local SiO_2 undersaturation (Erdenebayar et al. 2014). The comparable Al and Ti contents in UST quartz from the magmatic-hydrothermal transitional stage relative to the magmatic dendritic quartz indicate similar pH and temperature conditions during the formation of these quartz generations (Rusk et al. 2008; Huang and Audétat 2012). Alternatively, UST quartz may retain the trace element characteristics of the magmatic dendritic quartz, as supported by abundant primary melt inclusion in UST quartz (Yang et al. 2015). It has been noted from experiments that the Al contents of hydrothermal quartz also depend on

381 the ionized Al in the fluid, which increases with decreasing fluid pH (Rusk et al. 2008;
382 Müller et al. 2010; Li et al. 2020). Overall, the Al contents increase from the
383 magmatic-hydrothermal transitional (UST quartz) to the hydrothermal stage (BQ1 and
384 BQ2), suggesting that the pH gradually decreased during the fluid evolution (Fig. 6a).
385 The similar Ti contents indicate that the formation and chemistry of UST quartz were
386 probably also affected by rapid crystal growth (Huang and Audétat 2012; Cernuschi et al.
387 2018). Consequently, the lowest Ti contents were used for the temperature estimates to
388 avoid any overestimation (Huang and Audétat 2012; Cernuschi et al. 2018). This
389 approach yielded a temperature of ~700 °C for UST quartz, which is in the range of
390 related hypersaline primary fluid inclusion data (>600 °C, Qiao et al. 2022). The
391 suggested temperatures are also comparable with those of UST quartz from the Qulong
392 Cu-Mo deposit, China (600-700 °C; Qu et al. 2017) and Saginaw Hill porphyry Cu
393 system, USA (~650 °C; Bain et al. 2022).

394 Gray banded vein quartz (BQ) in porphyry deposits shows several consistent CL
395 characteristics in successive generations (e.g., Butte, Montana, Rusk and Reed 2002;
396 Bingham Canyon, Utah, Landtwing and Pettke 2005; Oyu Tolgoi, Mongolia, Müller et al.
397 2010; Altar, Argentina, Maydagán et al. 2015; Dabaoshan, China, Mao et al. 2017;
398 Haquira East, Peru, Cernuschi et al. 2018; Taiyangshan, China, Qiu et al. 2021). The
399 earliest BQ generation commonly exhibits CL-bright intensities and homogeneous
400 granular mosaic textures that lack internal growth zoning. By contrast, the subsequent BQ

401 generations commonly show darker CL intensities according to their lower Ti contents
402 compared to the earlier CL bright BQ (Mao et al. 2017; Cernuschi et al. 2018; Qiu et al.
403 2021). At Bilihe, the homogeneous CL texture of BQ1 is consistent with the observations
404 of BQ from the aforementioned porphyry deposits (Figs. 5g-h), which result from
405 relatively rapid nucleation and precipitation (e.g., Mao et al. 2017). Also, the mosaic
406 texture of BQ1 is indicative of the transition from lithostatic to hydrostatic pressure
407 conditions, and rapid quartz growth is likely a product of depressurization (Rusk and
408 Reed, 2002; Rusk 2012). High CL intensity of BQ2 with variable CL characteristics
409 along growth zones (Figs. 5g-h) implies rapid crystallization on a disturbed surface
410 (Gotte et al. 2011). In addition, the sharp boundaries in CL intensity among oscillating
411 growth zones indicate minimal trace element diffusion or reprecipitation after initial
412 quartz crystallization (Mao et al. 2017). Homogeneous mosaic texture was also observed
413 for BQ3, but with lower CL intensity and trace element concentrations compared to the
414 former BQ types (Figs. 5 and 6). The increasing Al from dendritic quartz to BQ2
415 indicates decreasing fluid pH, which agrees with the generally suggested pH decrease
416 during porphyry evolution (Beane and Titley 1981; Seedorff et al. 2005). By contrast, the
417 drop in the Al content from BQ2 to BQ3 suggests a relatively fast increase in fluid pH
418 possibly related to sericitic alteration that surrounds the BQ veins, which consumes H^+
419 from the fluid upon host rock sericitization (Rusk et al. 2008; Müller et al. 2010; Li et al.
420 2020). Due to the fast crystal growth of BQ, we also used the minimum Ti contents for

421 the temperature estimates yielding 635 °C for BQ1, 600 °C for BQ2, and 575 °C for BQ3
422 (Huang and Audétat 2012), which agrees with the upper-temperature limit (550 to 625 °C)
423 revealed by alteration mineral stabilities in sericitic alteration zones (e.g., Seedorff et al.
424 2005). By contrast, the temperatures of fluid inclusion in BQ are substantially lower
425 (~300-400 °C, Qiao et al. 2022), which we refer to the measurement of secondary fluid
426 inclusions modified by post-entrapment processes.

427 The CL-bright core of CQ appears to have embayed edges against the overgrown
428 rim, implying the dissolution of the core prior to recrystallization of the later rim (Rusk
429 2012). This is supported by distinct Ca concentrations (laser pits 3 and 8 in Fig. 8b) at the
430 boundary between the core and rim. Such dissolution textures were recognized in other
431 porphyry deposits (Maydagán et al. 2015; Mao et al. 2017; Qiu et al. 2021), and the
432 small-scale dissolution and re-equilibration of pre-existing quartz can be caused by
433 overprinting of late to post-magmatic fluids along micro-cracks or around fluid inclusions
434 (Erdenebayar et al. 2014). The highest Al concentrations are displayed in CQ among all
435 types of quartz, demonstrating increasing fluid acidity in accordance with the muscovite
436 and argillic alteration. Formation temperatures of ~250 °C were estimated by Ti in CQ
437 (Supplemental Table S2), which also agrees with typical argillic alteration temperatures
438 (<300 °C; Beane and Titley 1981; Seedorff et al. 2005), possibly reflecting the transition
439 to epithermal conditions. Additionally, CQ shows elevated contents of Li and Sb, which
440 indicates that a significant amount of these elements is more likely to be incorporated into

This is the peer-reviewed, final accepted version for American Mineralogist, published by the Mineralogical Society of America.
The published version is subject to change. Cite as Authors (Year) Title. American Mineralogist, in press.
DOI: https://doi.org/10.2138/am-2022-8840. http://www.minsocam.org/

441 epithermal quartz at lower temperatures (<300 °C; Jourdan et al. 2009).

442 In summary, the trace element characteristics of the different quartz-types from
443 Bilihe indicate decreasing quartz formation temperatures from magmatic dendritic quartz
444 at ~750 °C to CQ at ~250 °C, which marks the epithermal transition. In analogy, we
445 conclude that Al can be used as a tracer for fluid pH, indicating a general decrease in
446 fluid pH with porphyry evolution, except for BQ3, which agrees with the consecutive
447 alteration assemblages.

448

449 **Substitution mechanisms**

450 The atomic structure of the quartz lattice consists of strong Si-O bonds and the small
451 size of the Si^{4+} ion leads to its simple chemical composition with a relatively low capacity
452 for trace element incorporation (Götze 2009; Rusk 2012; Götze et al. 2021). However,
453 different mechanisms of trace element uptake into quartz may occur for some elements,
454 such as Ti, Al, Li, and K (Götze 2009), which is generally governed by substitution into
455 the crystal structure, interstitial atoms or species, and micro-inclusions (i.e., fluid or
456 mineral inclusions) in defects of the crystal (Jacamon and Larsen 2009). There are three
457 possible mechanisms for trace element incorporation into the quartz lattice (Götze et al.
458 2004; Larsen et al. 2004; Jacamon and Larsen 2009; Jourdan et al. 2009): (1) Si^{4+} can be
459 directly replaced by Ti^{4+}, Ge^{4+}; (2) two neighboring Si atoms in tetrahedral coordination
460 can be replaced by coupled substitution of P^{5+} together with trivalent Al^{3+} (Fe^{3+} or B^{3+});

This is the peer-reviewed, final accepted version for American Mineralogist, published by the Mineralogical Society of America.
The published version is subject to change. Cite as Authors (Year) Title. American Mineralogist, in press.
DOI: https://doi.org/10.2138/am-2022-8840. http://www.minsocam.org/

(3) Al^{3+}, Fe^{3+}, Ga^{3+} accommodate in quartz with monovalent cations (Li^{+}, Na^{+}, K^{+}, H^{+}, Rb^{+} or Cs^{+}) that compensate the charge deficit or enter interstices in structural channels that occur parallel to the c-axis of the quartz crystal (Jourdan et al. 2009).

Although the atomic Al: K or Al: Li ratios deviate from the 1:1 line (Fig. 9a), Al concentrations positively correlate (R^2=0.75) with the K concentration in dendritic quartz, UST quartz, and BQ, referring to a coupled $Si^{4+} \leftrightarrow (Al^{3+}) + (K^{+})$ element exchange vector (e.g., Götze et al. 2004; Hong et al. 2019). For CQ, the Al concentration correlates positively with Li (R^2=0.58), Rb (R^2=0.51), and Sb (R^2=0.65) concentrations (Figs. 9b-d), suggesting that these elements are incorporated into low-temperature quartz as charge-compensated cations in the substitution of $Si^{4+} \leftrightarrow (Al^{3+}, Sb^{3+}) + (Li^{+}, Rb^{+})$ (Götze et al. 2004; Larsen et al. 2004; Rusk et al. 2008). Boron, Sb, Ge, and As concentrations are little influenced by mineral inclusions, as their concentrations are commonly very low (<few ppm) in most common minerals in porphyry systems (Rottier and Casanova 2020). A positive correlation (R^2=0.49) is also observed between Al and B except for CQ, supporting that B^{3+} is present via coupled substitution with P^{5+} replacing two neighboring Si atoms (Fig. 9e; Jourdan et al. 2009). The weak correlation between Ge and Al (Fig. 9f) indicates that Ge and Al are not incorporated in quartz via a coupled substitution mechanism (Li et al. 2020).

Porphyry quartz as archives for the nature of Au deposition

This is the peer-reviewed, final accepted version for American Mineralogist, published by the Mineralogical Society of America.
The published version is subject to change. Cite as Authors (Year) Title. American Mineralogist, in press.
DOI: https://doi.org/10.2138/am-2022-8840. http://www.minsocam.org/

Hydrofracturing in the intrusion cupola is a critical process in porphyry systems, providing fluid pathways, which subsequently leads to the formation of mineralized veins and alteration features as a result of water-rock interaction (e.g., Sillitoe 2010; Pirajno and Zhou 2015; Cao et al. 2019; Tosdal and Dilles 2020; Qiu et al. 2021). Stockwork veins in porphyry deposits commonly consist of multiple quartz generations identified by distinct textures (Rusk and Reed 2002; Bennett 2014, Mao et al. 2017; Pan et al. 2019; Qiu et al. 2021). Hence, understanding the formation conditions of different quartz-types can help to reconstruct the crystallization history of minerals and reveal geological processes (Breitera et al. 2017; Götze et al. 2021).

Three stages of Au deposition reflecting distinct formation conditions can be distinguished at Bilihe according to the observations in this study and in combination with previous results (Yang et al. 2015; Qiao et al. 2022). This includes (1) Au related to the magmatic stage (~750 °C), where the round shape of the Au droplets is indicative for the presence of Au melts that were incorporated in the dendritic quartz during undercooling (Figs. 4a-b; Yang et al. 2015; Jian et al. 2021, 2022). A later-stage hydrothermal formation seems to be unlikely, as Au droplets are not related to fractures and occur within dense domains of dendritic quartz. This suggests that the magma was Au saturated, as evidenced by the Au enrichment (~26.3 ppb) in fresh magmatic rocks from the Bainaimiao Group (Yang et al. 2016) compared to average continental crust (~2.5 ppb; Wedepohl 1995). (2) Similar Au droplets were observed in BQ quartz (Fig.

501 4h-i), and we conclude, according to Jian et al. (2021, 2022), that the Au melt droplets
502 were transported in the high-temperature fluids (~600 °C) from which the BQ formed. (3)
503 By contrast, Au of hydrothermal nature is typically related to fractures in BQ, where it
504 coexists with sulfides and tennantite-tetrahedrite (Figs. 4f, j, 5f), or is found in the altered
505 host rocks (Fig. 4l).

506 Although Au-bearing dendritic and UST quartz exhibit a high average Au grade of
507 ~15.0 g/t in the Bilihe deposit, they are estimated to only hold less than one-third of the
508 total Au reserves (~8 tonnes; Qiao et al. 2022). By contrast, the auriferous BQ veinlets
509 host over 20 tonnes of the Au reserves (Qiao et al. 2022), implying that significant
510 amounts of the total Au reserves are rather associated with hydrothermal quartz formation
511 rather than with magmatic quartz formation. Thus, integrated information regarding the
512 morphology, CL characteristics, and trace element signatures of hydrothermal BQ1 to
513 BQ3 were used to reconstruct the formation history of the veinlets and the associated
514 precipitation conditions of Au (Fig. 10). This provides insights into the progressive
515 evolution of the Bilihe hydrothermal system and the related Au precipitation mechanisms.

516 The gray banded veins hosting BQ1 to BQ3 are mainly distributed in the
517 granodiorite porphyry and tuff. As mentioned above, fluids flow through fractures or
518 narrow pathways initially developed in the porphyry rocks due to hydrofracturing
519 associated with the magmatic-hydrothermal fluid ascent. Smaller equigranular
520 CL-homogeneous quartz crystals (BQ1; Fig. 5g) rapidly nucleated and precipitated on

their basal plane with various orientations, because of random nucleation along the walls of the fractures, which is in contrast to the common symmetric quartz formation towards the central vein suture (Fig. 10a; Penniston-Dorland 2001; Qiu et al. 2021). The later large and symmetric euhedral to subhedral CL-bright quartz crystals (BQ2; Fig. 5g) are oriented almost perpendicular to the vein wall and point towards the vein center (Fig. 10b), which overprint the preexisting randomly oriented BQ1. These BQ2 crystals display CL-concentric and sector growth zones along the c-axis (Fig. 10b), which crystallized from more acidic fluids indicated by their higher Al concentration relative to BQ1 (Fig. 6a). Shifts in fluid composition, pressure, temperature, precipitation rate, and/or a turbulent fluid flow regime resulted in rapid deposition of BQ2 with complex growth zonings (Roedder 1984). Gold mainly precipitated accompanying the formation of BQ1 and BQ2. Subsequently, the BQ3 formed as smaller sub-grains with lower CL intensity (Fig. 5g) and slightly lower trace element contents (Fig. 10c). The growth of BQ3 is related to increasing pH and decreasing temperature, as indicated by its Al and Ti contents, which was probably caused by mixing of porphyry fluid with meteoric water. Thereafter, the gray banded vein may be reopened and the post-ore calcite veinlets precipitated along the center (Fig. 10d).

In summary, quartz chemistry and CL textures of successive generations of quartz are controlled by the physical and chemical evolution of fluids in porphyry systems (Mao et al. 2017; Qiu et al. 2021). Within a specific quartz veinlet, the sequence of

chronological events detected by CL with trace element concentrations can further evaluate potential physiochemical fluctuations in the hydrothermal fluids (Qiu et al. 2021).

Comparison with quartz from other porphyry systems

Trace element compositions of quartz can be applied to fingerprint different types of ore formation and to decipher the fluid evolution of magmatic-hydrothermal ore deposits. For example, Rusk (2012) used Ti and Al concentrations and Al/Ti ratios to discriminate porphyry-type deposits, orogenic Au deposits, and epithermal deposits. It is also reported that the Ge/Al ratios can be used to distinguish magmatic and hydrothermal quartz (Müller et al. 2018). Rottier and Casanova (2020) proposed that trace element contents and ratios vary systematically between quartz from different porphyry vein-types. As a consequence, we conclude that compiled trace element data of quartz may help to distinguish between porphyry Cu, Mo, and Au sub-types (Fig. 11). Here, we present a compilation of ~1800 trace element compositions of quartz from different porphyry systems. This includes data from 1 porphyry Au-only deposit (this study), 6 porphyry Cu deposits (Butte, Los Pelambres, El Teniente, El Salvador, Santa Rita, and Haquira East), 1 porphyry Mo deposit (Dabaoshan), 5 porphyry Cu-Au deposits (Far Southeast, Central Oyu Tolgoi, Zesen Uul, Grasberg, and North Parkes), 1 porphyry Cu-Mo deposit (Yuanzhuding), and 3 porphyry Cu-Au-Mo deposits (Bingham, Altar, and Cerro de Pasco)

(Fig. 11; Supplemental Tables S3 and S4). We note that the following classification of the porphyry sub-types presented here refers to the studies from which the quartz data was extracted. We selected Al, Ti, Li, K, Ge, and Sb to define binary discrimination diagrams since these elements are commonly analyzed due to their relatively high abundance in quartz, and their systematic variations between the different porphyry sub-types (Fig. 11).

Collectively, we found that Ti, Al, Li, and K, as well as Ge/Ti and Al/Ti can be used to discriminate the different porphyry sub-types (Fig. 11). Despite some compositional overlaps, Ti, Al, Li, K, and Ge concentrations in quartz decrease from Au or Cu-Au to Cu-Mo and Mo porphyry deposits (Figs. 11a-c). Although, there seems to be an overall Ti decrease from porphyry Au-only to porphyry Mo deposits (Fig. 11a), however, temperature control on the Ti variation seems to be unlikely in this case, as temperature does not vary systematically between porphyry sub-types (Barton et al. 2020). By contrast, Al and Li concentrations increase in quartz with decreasing pressure conditions (Rambourg et al. 2022), and it is known that Au-only porphyries tend to form at shallower crustal levels compared to their Cu and Mo counterparts (Murakami et al. 2009; Sillitoe 2017). Hence, the decreasing Li and Al contents in quartz from porphyry Au-only to Mo deposits reflect the distinct formation of these porphyry sub-types (Fig. 11b). In addition, porphyry Au-only and Cu-Au deposits exhibit higher K concentrations in quartz compared to porphyry Mo deposit (Fig. 11c). Generally, quartz form porphyry Au or Cu-Au deposits show little variation in their Ge concentrations (2-10 ppm), whilst quartz

581 from porphyry Mo or Cu-Mo deposits show a much broader Ge range (0.26-28.6 ppm,
582 Fig. 11d). Finally, most quartz from porphyry Mo or Cu-Mo deposits shows higher Ge/Ti
583 and Al/Ti ratios than those from Au-only or Cu-Au porphyries (Fig. 11d). Although the
584 processes that control the trace element variations in quartz between porphyry sub-types
585 on the global scale remain elusive and require more detailed investigation, which is out of
586 scope of this study, we showed that trace elements in quartz are suitable to discriminate
587 between porphyry sub-types and that Li and Al in quartz vary with respect to porphyry
588 formation depth.
589

590 **IMPLICATIONS**

591 This study reports the distinctive SEM-CL textures and trace element contents of
592 four quartz generations recording the fluid evolution from the magmatic to hydrothermal
593 stages in the Bilihe porphyry Au-only deposit, NE China. The application of CL textures
594 combined with trace element data of successive quartz generations can advance the
595 comprehension of the relation between CL intensities and quartz chemistry, trace element
596 substitution in quartz, and the specific ore-forming physiochemical environments.
597 Additionally, we note that temperature estimates by Ti-in-quartz geothermometry are
598 sensitive to overestimation in porphyry environments due to rapid growth rate of quartz,
599 which must therefore be handled with care. Finally, it is of broad significance to apply
600 compiled trace element compositions and ratios of quartz to predict metal fertility of

601 porphyry mineralization. We address that the processes that cause these global trace
602 element variations between porphyry sub-types require further investigation, but Li and
603 Al seem to be particularly suitable to record relative changes in porphyry formation
604 depth.
605

606 ## ACKNOWLEDGEMENTS

607 This research was supported financially by the National Natural Science Foundation
608 of China (Grants 42122012 and 92062219), the Inner Mongolia Academician Project
609 (Grant 2022-TZH03), and the China Scholarship Council (CSC; File No. 202206400014).
610 We thank Li Su and Hongyu Zhang (CUGB) for the quartz trace element analyses, and
611 Junfeng Shen (CUGB) for the quartz SEM-CL analyses. Sincere thanks are given to John
612 Dilles, another two anonymous reviewers, and Associate Editor Daniel Gregory for their
613 constructive comments and editing, which greatly improved this work.
614

615 ## REFERENCES

616 Bain, W.M., Lecumberri-Sanchez, P., Marsh, E.E., and Steele-MacInnis, M. (2022) Fluids
617 and melts at the magmatic-hydrothermal transition, recorded by Unidirectional
618 Solidification Textures at Saginaw Hill, Arizona, USA. Economic Geology, 117(7),

619 1543-1571.

620 Barton, I. F., Rathkopf, C. A., and Barton, M. D. (2020) Rhenium in molybdenite: a
621 database approach to identifying geochemical controls on the distribution of a
622 critical element. Mining, Metallurgy and Exploration, 37, 21-37.

623 Beane, R., and Titley, S. (1981) Part I. Geologic Settings, Petrology, and Tectogenesis.
624 Society of Economic Geologists, Seventy-Fifth Anniversary Volume, Brian J.
625 Skinner.

626 Bennett, M.M. (2014) Cathodoluminescence and fluid inclusion characteristics of
627 hydrothermal quartz from porphyry deposits. 162 p. Master thesis, Colorado School
628 of Mines, Colorado.

629 Breiter, K., Ďurišová, J., and Dosbaba, M. (2017) Quartz chemistry–A step to
630 understanding magmatic-hydrothermal processes in ore-bearing granites:
631 Cínovec/Zinnwald Sn-W-Li deposit, Central Europe. Ore Geology Reviews, 90,
632 25-35.

633 Cao, K., Yang, Z., Mavrogenes, J., White, N., Xu, J., Li, Y., and Li, W. (2019) Geology
634 and genesis of the giant Pulang porphyry Cu-Au district, Yunnan, Southwest China.
635 Economic Geology, 114(2), 275-301.

636 Cernuschi, F., Dilles, J.H., Grocke, S.B., Valley, J.W., Kitajima, K., and Tepley, F.J. (2018)
637 Rapid formation of porphyry copper deposits evidenced by diffusion of oxygen and
638 titanium in quartz. Geology, 46(7), 611-614.

639 Erdenebayar, J., Ogata, T., Imai, A., and Sereenen, J. (2014) Textural and chemical
640 evolution of Unidirectional Solidification Textures in highly differentiated granitic
641 rocks at Kharaatyagaan, Central Mongolia. Resource Geology, 64(4), 283-300.
642 Frelinger, S. N., Ledvina, M. D., Kyle, J. R., and Zhao, D. (2015) Scanning electron
643 microscopy cathodoluminescence of quartz: Principles, techniques and applications
644 in ore geology. Ore Geology Reviews, 65, 840-852.
645 Gao, S., Zou, X., Hofstra, A., Qin, K., Marsh, E., Bennett, M., Li, G., Jiang, J., Su, S.,
646 Zhao, J., and Li, Z. (2022) Trace elements in quartz: insights into source and fluid
647 evolution in magmatic-hydrothermal systems. Economic Geology, 117(6),
648 1415-1428.
649 Ge, L., Qin, M., Zhang, W., Yuan, S., Duan, X., Ma, M., Pan, J., and Tang, M. (2009) The
650 Bilihei gold deposit in Inner Mongolia: the first large-sized high-grade concealed
651 porphyry Au deposit discovered on the northern margin of North China plate.
652 Geology in China, 36(5), 1110-1122 (in Chinese with English abs.).
653 Gotte, T., Pettke, T., Ramseyer, K., Koch-Muller, M., and Mullis, J. (2011)
654 Cathodoluminescence properties and trace element signature of hydrothermal quartz:
655 A fingerprint of growth dynamics. American Mineralogist, 96(5-6), 802-813.
656 Götze, J., Plötze, M., Graupner, T., Hallbauer, D.K., and Bray, C.J. (2004) Trace element
657 incorporation into quartz: A combined study by ICP-MS, electron spin resonance,
658 cathodoluminescence, capillary ion analysis, and gas chromatography. Geochimica

et Cosmochimica Acta, 68(18), 3741-3759.

Götze, J. (2009) Chemistry, textures and physical properties of quartz-geological interpretation and technical application. Mineralogical Magazine, 73(4): 645-671.

Götze, J., Schertl, H.P., Neuser, R.D., Kempe, U., and Hanchar, J.M. (2012) Optical microscope-cathodoluminescence (OM-CL) imaging as a powerful tool to reveal internal textures of minerals. Mineralogy and Petrology, 107(3), 373-392.

Götze, J., Pan, Y., and Müller, A. (2021) Mineralogy and mineral chemistry of quartz: A review. Mineralogical Magazine, 85(5), 639-664.

Hong, J.X., Zhang, H.Y., Zhai, D.G., Li, D.F., Zhang, Y.L., and Liu, J.J. (2021) The geochronology of the Haobugao skarn Zn-Pb deposit (NE China) using garnet LA-ICP-MS U-Pb dating. Ore Geology Reviews, 139, 104437.

Hong, W., Cooke, D.R., Zhang, L., Fox, N., and Thompson, J. (2019) Cathodoluminescence features, trace elements, and oxygen isotopes of quartz in unidirectional solidification textures from the Sn-mineralized Heemskirk Granite, western Tasmania. American Mineralogist, 104(1), 100-117.

Huang, K., Zhu, M., Zhang, L., Bai, Y., and Cai, Y. (2020) Geological and mineralogical constraints on the genesis of the Bilihe gold deposit in Inner Mongolia, China. Ore Geology Reviews, 124, 103607.

Huang, R., and Audétat, A. (2012) The titanium-in-quartz (TitaniQ) thermobarometer: A critical examination and re-calibration. Geochimica et Cosmochimica Acta, 84,

679 75-89.

680 Jacamon, F., and Larsen, R.B. (2009) Trace element evolution of quartz in the
681 charnockitic Kleivan granite, SW-Norway: The Ge/Ti ratio of quartz as an index of
682 igneous differentiation. Lithos, 107(3-4), 281-291.

683 Jahn, B.M. (2004) The Central Asian Orogenic Belt and growth of the continental crust in
684 the Phanerozoic. In: Malpas, J., Fletcher, C.J.N., Ali, J.R., Aitchison, J.C. (Eds.),
685 Aspects of the tectonic evolution of China. Geological Society London Special
686 Publications, 226, 73-100.

687 Jian, W., Mao, J., Lehmann, B., Cook, N.J., Xie, G., Liu, P., Duan, C., Alles, J., and Niu,
688 Z.J. (2021) Au-Ag-Te-rich melt inclusions in hydrothermal gold-quartz veins,
689 Xiaoqinling lode gold district, central China. Economic Geology, 116(5),
690 1239-1248.

691 Jian, W., Mao, J., Cook, N.J., Chen, L., Xie, G., Xu, J., Song, S., Hao, J., Li, R., and Liu,
692 J. (2022) Intracrystalline migration of polymetallic Au-rich melts in multistage
693 hydrothermal systems: example from the Xiaoqinling lode gold district, central
694 China. Mineralium Deposita, 57(2), 147-154.

695 Jourdan, A., Mullis, J., Ramseyer, K., and Spiers, C.J. (2009) Evidence of growth and
696 sector zoning in hydrothermal quartz from Alpine veins. European Journal of
697 Mineralogy, 21(1), 219-231.

698 Landtwing, M., and Pettke, T. (2005) Relationships between SEM-cathodoluminescence

699 response and trace-element composition of hydrothermal vein quartz. American
700 Mineralogist, 90(1), 122-131.
701 Larsen, R.B., Henderson, I., Ihlen, P.M., and Jacamon, F. (2004) Distribution and
702 petrogenetic behaviour of trace elements in granitic pegmatite quartz from South
703 Norway. Contributions to Mineralogy and Petrology, 147(5), 615-628.
704 Li, J., Hu, R., Xiao, J., Zhuo, Y., Yan, J., and Oyebamiji, A. (2020) Genesis of gold and
705 antimony deposits in the Youjiang metallogenic province, SW China: Evidence from
706 in situ oxygen isotopic and trace element compositions of quartz. Ore Geology
707 Reviews, 116, 103257.
708 Li, W., Qiao, X., Zhang, F., and Zhang, L. (2021) Tourmaline as a potential mineral for
709 exploring porphyry deposits: a case study of the Bilihe gold deposit in Inner
710 Mongolia, China. Mineralium Deposita, 57(1), 61-82.
711 Li, Y., She, Z., and Ma, C. (2011) SEM-CL analysis of quartz and its application in
712 petrology. Advances in Earth Science, 26(3), 325-331 (in Chinese with English
713 abs.).
714 Liu, C., and Nie, F. (2015) Permian magmatic sequences of the Bilihe gold deposit in
715 central Inner Mongolia, China: Petrogenesis and tectonic significance. Lithos, 231,
716 35-52.
717 Liu, J.F., Li, J.Y., Chi, X.G., Qu, J.F., Hu, Z.C., Fang, S., and Zhang, Z. (2013) A
718 late-Carboniferous to early early-Permian subduction-accretion complex in Daqing

719 pasture, southeastern Inner Mongolia: evidence of northward subduction beneath the
720 Siberian Paleoplate southern margin. Lithos, 177, 285-296.
721 Liu, J., Wang, C., Liu, Y., Zhang, H., Ge, J., and Li, S. (2019) Middle Permian Wuhaolai
722 mafic complex in the northern North China Craton: Constraints on the
723 subduction-related metasomatic mantle and tectonic implication. Geological Journal,
724 54(4), 1834-1852.
725 Lowenstern, J.B., and Sinclair, W.D. (1996) Exsolved magmatic fluid and its role in the
726 formation of comb-layered quartz at the Cretaceous Logtung W-Mo deposit, Yukon
727 Territory, Canada. Earth and Environmental Science Transactions of the Royal
728 Society of Edinburgh, 87(1-2), 291-303.
729 Mao, W., Rusk, B., Yang, F., and Zhang, M.J. (2017) Physical and chemical evolution of
730 the Dabaoshan porphyry Mo deposit, South China: Insights from fluid inclusions,
731 cathodoluminescence, and trace elements in quartz. Economic Geology, 112(4),
732 889-918.
733 Maydagán, L., Franchini, M., Rusk, B., Lentz, D.R., McFarlane, C., Impiccini, A., Ríos,
734 F.J., and Rey, R.J. (2015) Porphyry to epithermal transition in the Altar Cu-(Au-Mo)
735 deposit, Argentina, studied by cathodoluminescence, LA-ICP-MS, and fluid
736 inclusion analysis. Economic Geology, 110(4), 889-923.
737 Murakami, H., Seo, J.H., and Heinrich, C.A. (2009) The relation between Cu/Au ratio
738 and formation depth of porphyry-style Cu–Au ± Mo deposits. Mineralium Deposita,

739 45(1), 11-21.

740 Müller, A., Herrington, R., Armstrong, R., Seltmann, R., Kirwin, D.J., Stenina, N.G., and
741 Kronz, A. (2010) Trace elements and cathodoluminescence of quartz in stockwork
742 veins of Mongolian porphyry-style deposits. Mineralium Deposita, 45(7), 707-727.

743 Müller, A., Herklotz, G., and Giegling, H. (2018) Chemistry of quartz related to the
744 Zinnwald/Cínovec Sn-W-Li greisen-type deposit, Eastern Erzgebirge, Germany.
745 Journal of Geochemical Exploration, 190, 357-373.

746 Nie, F., and Bjørlykke, A. (1999) Nd and Sr isotope constraints on the age and origin of
747 Proterozoic meta-mafic volcanic rocks in the Bainaimiao-Wenduermiao district,
748 south-central Inner Mongolia, China. Continental Dynamics, 4(1), 1-14.

749 Pan, J.Y., Ni, P., and Wang, R.C. (2019) Comparison of fluid processes in coexisting
750 wolframite and quartz from a giant vein-type tungsten deposit, South China: Insights
751 from detailed petrography and LA-ICP-MS analysis of fluid inclusions. American
752 Mineralogist, 104(8), 1092-1116.

753 Peng, H., Wang, X., Tang, J., and Wang, D. (2010) The application of quartz
754 cathodoluminescence in study of igneous rock. Rock and Mineral Analysis, 29(2),
755 153-160 (in Chinese with English abs.).

756 Penniston-Dorland, S.C. (2001) Illumination of vein quartz textures in a porphyry copper
757 ore deposit using scanned cathodoluminescence: Grasberg Igneous Complex, Irian
758 Jaya, Indonesia. American Mineralogist, 86(5-6), 652-666.

759 Pirajno, F., and Zhou, T.F. (2015) Intracontinental porphyry and porphyry-skarn mineral
760 systems in Eastern China: Scrutiny of a special case “Made-in-China”. Economic
761 Geology, 110, 603-629.
762 Qiao, X., Li, W., Zhang, L., Zhang, F., Zhu, X., and Xia, X. (2022) Textural, fluid
763 inclusion, and in-situ oxygen isotope studies of quartz: Constraints on vein
764 formation, disequilibrium fractionation, and gold precipitation at the Bilihe gold
765 deposit, Inner Mongolia, China. American Mineralogist, 107(3), 517-531.
766 Qing, M., Tang, M., Ge, L., Han, X., Feng, J., Yuan, S., and Zhao, Y. (2012) LA-ICP-MS
767 zircon U-Pb age, geochemistry of andesite in Bilihe goldfield, Suniteyouqi, Inner
768 Mongolia and its tectonic significance. Acta Petrologica Sinica, 28(2), 514-524 (in
769 Chinese with English abs.).
770 Qiu, K., Deng, J., Yu, H., Wu, M., Wang, Y., Zhang, L., and Goldfarb, R. (2021)
771 Identifying hydrothermal quartz vein generations in the Taiyangshan porphyry
772 Cu-Mo deposit (West Qinling, China) using cathodoluminescence, trace element
773 geochemistry, and fluid inclusions. Ore Geology Reviews, 128, 103882.
774 Qu, H., Sun, M., and Dong, P. (2017) The $\delta^{18}O$ of UST quartz in two porphyry deposits,
775 China. Resource Geology, 67(1), 109-115.
776 Raimbourg H., Famin V., Canizarès A., and Trong L. (2022) Fluid pressure changes
777 recorded by trace elements in quartz. Geochemistry, Geophysics, Geosystems,
778 23(10), e2022GC010346.

779 Redmond, P. B., Einaudi, M. T., Inan, E. E., Landtwing, M. R., and Heinrich, C. A. (2004)
780 Copper deposition by fluid cooling in intrusion-centered systems: New insights from
781 the Bingham porphyry ore deposit, Utah. Geology, 32(3), 217-220.
782 Roedder, E. (1984) Fluid Inclusions: Reviews in Mineralogy, Washington. D.C,
783 Mineralogical Society of America, 646.
784 Rottier, B., and Casanova, V. (2020) Trace element composition of quartz from porphyry
785 systems: a tracer of the mineralizing fluid evolution. Mineralium Deposita, 56(5),
786 843-862.
787 Rusk, B.G., and Reed, M. (2002) Scanning electron microscope–cathodoluminescence
788 analysis of quartz reveals complex growth histories in veins from the Butte porphyry
789 copper deposit, Montana. Geology, 30(8), 727-730.
790 Rusk, B.G., Reed, M. H., Dilles, J. H., and Kent, A. J. R. (2006) Intensity of quartz
791 cathodoluminescence and trace-element content in quartz from the porphyry copper
792 deposit at Butte, Montana. American Mineralogist, 91(8-9), 1300-1312.
793 Rusk, B.G., Lowers, H.A., and Reed, M.H. (2008) Trace elements in hydrothermal quartz:
794 Relationships to cathodoluminescent textures and insights into vein formation.
795 Geology, 36(7), 547-550.
796 Rusk, B., Koenig, A., and Lowers, H. (2011) Visualizing trace element distribution in
797 quartz using cathodoluminescence, electron microprobe, and laser
798 ablation-inductively coupled plasma-mass spectrometry. American Mineralogist,

96(5-6), 703-708.

Rusk, B.G. (2012) Cathodoluminescent textures and trace elements in hydrothermal quartz. In J. Götze and R. Möckel, Eds., Quartz: Deposits, Mineralogy and Analytics, p. 307-329. Springer, Berlin.

Schneider, C. A., Rasband, W. S., and Eliceiri, K. W. (2012) NIH Image to ImageJ: 25 years of image analysis. Nature Methods, 9(7), 671-675.

Seedorff, E., Dilles, J.H., Proffett, J.M., Einaudi, M.T., Zurcher, L., Stavast, W.J., Johnson, D.A., and Barton, M.D. (2005) Porphyry deposits: Characteristics and origin of hypogene features. Economic Geology, One Hundredth Anniversary Volume.

Sillitoe, R.H. (2010) Porphyry copper systems. Economic Geology, 105(1), 3-41.

Sillitoe RH (2017) Gold-rich porphyry deposits: types, settings, controls, and potential. In: Mineral resources to discover. Proc 14th SGA biennial meeting, Québec City, 1, 11-14.

Sun, S., and McDonough, W. (1989) Chemical and isotopic systematics of oceanic basalts: implications for mantle composition and processes. Geological Society London Special Publications, 42 (1), 313-345.

Swanson, S.E., and Fenn, P.M. (1986) Quartz crystallization in igneous rocks. American Mineralogist, 71(3-4), 331-342.

Tang, K., and Yan, Z. (1993) Regional metamorphism and tectonic evolution of the Inner Mongolian suture zone. Journal of Metamorphic Geology, 11(4), 511-522.

819 Tanner, D., Henley, R.W., Mavrogenes, J.A., and Holden, P. (2013) Combining in situ
820 isotopic, trace element and textural analyses of quartz from four
821 magmatic-hydrothermal ore deposits. Contributions to Mineralogy and Petrology,
822 166(4), 1119-1142.
823 Thomas, J.B., Bruce Watson, E., Spear, F.S., Shemella, P.T., Nayak, S.K., and Lanzirotti,
824 A. (2010) TitaniQ under pressure: the effect of pressure and temperature on the
825 solubility of Ti in quartz. Contributions to Mineralogy and Petrology, 160(5),
826 743-759.
827 Tosdal, R.M., and Dilles, J.H. (2020) Creation of permeability in the porphyry Cu
828 environment. Society of Economic Geologists, Special Publications. 21.
829 Wang, Y., Zeng, Q., Guo, L., and Guo, Y. (2019) Magmatic and tectonic setting of the
830 Permian Au mineralization in the Xing-Meng Orogenic Belt: constraints from the
831 U–Pb ages, Hf–O isotopes and geochemistry of granitic intrusions in the Bilihe and
832 Hadamiao gold deposits. Mineralogy and Petrology, 113, 99-118.
833 Wedepohl, K.H. (1995) The composition of the continental crust. Geochimica et
834 cosmochimica Acta, 59(7), 1217-1232.
835 Wiedenbeck, M., Alle, P., Corfu, F., Griffin, W., Meier, M., Oberli, F., Von Quadt, A.,
836 Roddick, J., and Spiegel, W. (1995) Three natural zircon standards for U-Th-Pb,
837 Lu-Hf, trace element and REE analyses. Geostandard Newsletter, 19, 1-23.
838 Wilde, S. (2015) Final amalgamation of the Central Asian orogenic belt in NE China:

839 Paleo-Asian Ocean closure versus Paleo-Pacific plate subduction—A review of the
840 evidence. Tectonophysics, 662, 345-362.

841 Wu, F., Sun, D., Ge, W., Zhang, Y., Grant, M., Wilde, S., and Jahn, B. (2011)
842 Geochronology of the Phanerozoic granitoids in northeastern China. Journal of
843 Asian Earth Sciences. 41 (1), 1-30.

844 Xiao, W., Windley, B.F., Hao, J., and Zhai, M. (2003) Accretion leading to collision and
845 the Permian Solonker suture, Inner Mongolia, China: Termination of the central
846 Asian orogenic belt. Tectonics, 22(6), 1609-1089.

847 Xiao, W.J., Nie, F.J., Liu, Y.F., and Liu, Y. (2012) Isotope geochronology study of the
848 granitoid intrusions in the Changshanhao gold deposit and its geological
849 implications. Acta Petrologica Sinica 28, 535-543 (in Chinese with English abs.).

850 Xu, B., Charvet, J., Chen, Y., Zhao, P. and Shi, G. (2013) Middle Paleozoic convergent
851 orogenic belts in western Inner Mongolia (China): Framework, kinematics,
852 geochronology and implications for tectonic evolution of the Central Asian Orogenic
853 Belt. Gondwana Research, 23(4), 1342-1364.

854 Xu, W., Pei, F., Wang, F., Meng, E., Ji, W., Yang, D., and Wang, W. (2013) Spatial
855 temporal relationships of Mesozoic volcanic rocks in NE China: constraints on
856 tectonic overprinting and transformations between multiple tectonic regimes. Journal
857 of Asian Earth Sciences. 74, 167-193.

858 Xu, B., Zhao, P., Bao, Q., Zhou, Y., Wang, Y., and Luo, Z. (2014) Preliminary study on

the pre-Mesozoic tectonic unit division of the Xing-Meng Orogenic Belt (XMOB). Acta Petrologica Sinica, 30(7), 1841-1857 (in Chinese with English abs.).

Xu, B., Zhao, P., Wang, Y., Liao, W., Luo, Z., Bao, Q., and Zhou, Y. (2015) The pre-Devonian tectonic framework of Xing'an–Mongolia orogenic belt (XMOB) in north China. Journal of Asian Earth Sciences, 97, 183-196.

Yang, Z., Hou, Z., Li, Z., Song, Y., and Xie, Y. (2008) Direct record of primary fluid exsolved from magma: Evidence from unidirectional solidification texture (UST)in quartz found in Qulong porphyry copper deposit, Tibet. Mineral Deposits, 27(2), 188-199 (in Chinese with English abs.).

Yang, Z., Chang, Z., Paquette, J., White, N.C., Hou, Z., and Ge, L. (2015) Magmatic Au mineralization at the Bilihe Au deposit, China. Economic Geology, 110(7), 1661-1668.

Yang, Z., Chang, Z., Hou, Z., and Meffre, S. (2016) Age, igneous petrogenesis, and tectonic setting of the Bilihe gold deposit, China, and implications for regional metallogeny. Gondwana Research, 34, 296-314.

Yang, Z., and Cooke, D. (2019) Porphyry copper deposits in China. Society of Economic Geologists, Special Publications, 22, 133-187.

Zhai, D., Williams-Jones, A.E., Liu, J., Selby, D., Li, C., Huang, X.W., Qi, L., and Guo, D. (2019) Evaluating the Use of the Molybdenite Re-Os Chronometer in Dating Gold Mineralization: Evidence from the Haigou Deposit, Northeastern China. Economic

879 Geology, 114(5), 897-915.

880 Zhai, D., Williams-Jones, A.E., Liu, J., Selby, D., Voudouris, P.C., Tombros, S., Li, K., Li,
881 P., and Sun, H. (2020) The genesis of the giant Shuangjianzishan epithermal
882 Ag-Pb-Zn deposit, Inner Mongolia, Northeastern China. Economic Geology, 115(1),
883 101-128.

884 Zhang, H., Liu, J.C., Xu, Q., and Wang, J.Y. (2020) Geochronology, isotopic chemistry,
885 and gold mineralization of the black slate-hosted Haoyaoerhudong gold deposit,
886 northern North China Craton. Ore Geology Reviews, 117, 103315.

887 Zhang, H., Su, L., Wang, J., Yang, L., Wang, D., Hu, X., Song, Y., and Xiong, L. (2019)
888 Study on LA-ICP-MS determination of trace elements in sulfide minerals. Hans
889 Journal of Chemical Engineering and Technology, 9(5), 401-409 (in Chinese with
890 English abs.).

891 Zhang, J.H., Gao, S., Ge, W.C., Wu, F.Y., Yang, J.H., Wilde, S.A., and Li, M. (2010)
892 Geochronology of the Mesozoic volcanic rocks in the Great Xing'an Range,
893 northeastern China: Implications for subduction-induced delamination. Chemical
894 Geology, 276(3-4), 144-165.

895 Zhang, S.H., Zhao, Y., Ye, H., Liu, J.M., and Hu, Z.C. (2014) Origin and evolution of the
896 Bainaimiao arc belt: Implications for crustal growth in the southern Central Asian
897 orogenic belt. Geological Society of America Bulletin, 126(9-10), 1275-1300.

898 Zhao, Q., Zhai, D., Mathur, R., Liu, J., Selby, D., Williams-Jones, A.E. (2021a) The giant

899 Chalukou porphyry Mo deposit, NE China: The product of a short-lived, high flux
900 mineralizing event. Economic Geology, 116 (5), 1209-1225.
901 Zhao, Q., Zhai, D., Wang, J., Liu, J., and Williams-Jones, A.E. (2021b) The geochemistry
902 and geochronology of Permian granitoids from central Inner Mongolia, NE China:
903 Petrogenesis and tectonic implications. Lithos, 404-405, 106489.
904 Zhao, Q., Zhai, D., Williams-Jones, A.E. and Liu, J. (2023) Trace element and isotopic (S,
905 Pb) constraints on the formation of the giant Chalukou porphyry Mo deposit, NE
906 China. American Mineralogist, 108(1): 160-177.
907 Zhu, M., Huang, K., Hu, L., Bai, Y.,Li, W., Gao, B., and Zhang, L. (2018) Zircon
908 U-Pb-Hf-O and molybdenite Re-Os isotopic constraints on porphyry gold
909 mineralization in the Bilihe deposit, NE China. Journal of Asian Earth Sciences, 165,
910 371-382.
911
912
913
914
915
916
917
918

919

920

921 **FIGURE CAPTIONS**

922 Figure 1. Regional geological map of the Bilihe deposit in NE China. (**a**) Tectonic map of
923 the Central Asian orogenic belt (CAOB; based on Jahn et al. 2004); (**b**) Simplified
924 geological map of part of the Xing-Meng Orogenic Belt (XMOB) showing the study area
925 (modified from Xu et al. 2014); (**c**) Tectonic map of central Inner Mongolia showing the
926 structures and tectonic belts (modified from Yang et al. 2016). Abbreviations: EB = the
927 Erguna block, XAB = the Xing'an-Airgin Sum block, SHB = the Songliao-Hunshandake
928 block; JB= and the Jiamusi block, XXS = Xinlin-Xiguitu suture, XHS = the
929 Xilinhot-Heihe suture, MS = the Mudanjiang suture, OYS = the Ondor Sum-Yongji
930 suture.

931

932 Figure 2. (**a**) Geological map of the Bilihe deposit showing main geologic units and faults
933 (modified from Ge et al. 2009). (**b**) Geological section along cross-section A-B through
934 the Center II orebody (modified from Wang et al. 2019).

935

936 Figure 3. Hand specimen photos and photomicrographs of different quartz generations
937 from the Bilihe Au deposit. (**a**) Well-preserved dendritic quartz hosted by granodiorite

porphyry. (**b**) Dendritic quartz in transmitted light. (**c**) Multi-layered comb UST quartz, and the yellow arrows towards the center of the granitic stocks. (**d**) UST quartz in transmitted light. (**e**) Sinuous K-feldspar vein cut by weakly curved gold-bearing BQ with local K-feldspar halo. (**f**) Dendritic quartz cut by BQ stockworks. (**g**) Contorted UST quartz layer showing basal, thin, finer-grained parts cut by BQ, with disseminated tourmaline alteration. (**h**) BQ stockworks cut by CQ with white to brown cement. Abbreviations: GDP = granodiorite porphyry, KV = K-feldspar vein, Tur = tourmaline.

Figure 4. Main gold-bearing units in the Bilihe gold deposit. (**a**) Isolated Au grains with hexagonal shape in dendritic quartz. (**b**) Gold trails of straight lines in dendritic quartz. (**c**) Irregular Au grains in UST quartz factures. (**d**) Irregular Au grains in UST quartz. (**e**) Isolated Au grains of droplet shape in UST quartz. (**f**) Irregular Au grains in UST quartz factures. (**g**) Irregular Au grains hosted in the interval of UST quartz. (**h**-**i**) Isolated Au grains of rounded shape in BQ. (**j**) Gold coexisting with tetrahedrite, chalcopyrite, and rutile in BQ. (**k**) Gold coexisting with pyrite, tennantite, and chalcopyrite along the facture in dendritic quartz. (**l**) Irregular Au grains in the adjacent sericitization zones. Abbreviations: Ccp = chalcopyrite, Py = pyrite, Rt = rutile, Ser = sericitization, Tnt = tennantite, Ttr = tetrahedrite.

Figure 5. The SEM-CL and *ImageJ*-processed images of different types of quartz in the

Bilihe gold deposit. (**a**-**b**) Dendritic quartz featured by sector-zoned with euhedral oscillatory growth zones of fine laminae of 5 to 100 μm in width that are parallel to grain edges. (**c**) Gold trails hosted in dendritic quartz consistent with the kink point of the CL-concentric zoning of the surrounding quartz. (**d**-**e**) Inhomogeneous growth fabrics with weak zoning and patchy luminescence in UST quartz. (**f**) UST quartz grains of CL-bright cores with CL-darker corrosion, and Au grains in the interspace of UST quartz crystals. (**g**-**h**) CL textures of gold-bearing BQ from both sides of the vein wall to the center, with the white lines marking the BQ3 zones. (**i**) Gold precipitated with pyrite. (**j**-**k**) CQ of CL-bright core and CL-dark to CL-bright growth zones with oscillating CL intensity in the rim. Abbreviations: Mag = magnetite.

Figure 6. Percentile box and whisker plots showing the trace element compositions of different quartz types from the Bilihe Au deposit. (**a**) Al, (**b**) Fe, (**c**) B, (**d**) Sb, (**e**) Li, (**f**) Ti, (**g**) Ge, (**h**) Mg, (**i**) Mn.

Figure 7. Chondrite-normalized REE patterns of dendritic quartz (**a**), UST quartz (**b**), BQ(**c**), and CQ (**d**) in the Bilihe Au deposit. Normalization values are from Sun and McDonough (1989).

Figure 8. The correlation between the CL intensity and trace element concentrations of Ti,

978 Al, K, and Ca in dendritic quartz (**a**) and CQ (**b**).

979

980 Figure 9. Concentrations of K, Li, Rb, B, Sb, and Ge versus Al in various types of quartz
981 from the Bilihe Au deposit.

982

983 Figure 10. Schematic diagram of the sequence of events juxtaposed in a single
984 hydrothermal quartz vein from the Bilihe porphyry Au deposit. Arrow points out the fluid
985 flow direction. Yellow dots represent Au grains. Light gray quartz represents BQ1, blue
986 quartz represents BQ2, and purple quartz represents BQ3. Veins are symmetrically
987 developed from vein wall to the center. Estimations of temperature and variations in Al,
988 Ti, Li, Sb contents (median values) of BQ1, BQ2, BQ3, and CQ are listed respectively.

989

990 Figure 11. Correlation diagrams of selected trace elements. (**a**) Al vs. Ti; (**b**) Al vs. Li; (**c**)
991 Al vs. K; (**d**) Al/ Ti vs. Ge/ Ti. Data are from Supplemental Table S3, Rottier and
992 Casanova (2020) and references therein. The black arrows indicate the variation between
993 different porphyry deposit sub-types (e.g., Au vs. Cu-Mo).

994

995 Table 1. Representative LA-ICP-MS trace element results of quartz from the Bilihe Au
996 deposit (ppm).

997

998 Supplemental Table S1. LA-ICP-MS analyses of quartz from the Bilihe porphyry gold
999 deposit (ppm).
1000 Supplemental Table S2. Summary of estimated Ti-in-quartz geothermometer
1001 temperatures from the Bilihe deposit.
1002 Supplemental Table S3. Compiled quartz trace element data from different porphyry ore
1003 systems (ppm).
1004 Supplemental Table S4. Summary of total tons of ore and the average grades of Cu, Mo,
1005 Au and Ag for the different deposits.
1006
1007
1008
1009
1010
1011
1012
1013
1014
1015
1016
1017

1018

1019

Table 1. Representative LA-ICP-MS trace element results of quartz from the Bilihe Au deposit (ppm)

Elements	Al	Li	Ti	K	B	Mg	Mn	Fe	Ge	Rb	Sb
Dendritic quartz (n=40)											
Min	163	5.59	74.6	22.5	2.74	10.1	1.55	101	2.14	0.29	0.18
Max	1576	71.1	440	920	31.8	459	18.8	330	7.50	4.11	6.70
Median	665	21.2	300	195	10.4	59.3	3.05	179	3.80	0.58	0.45
MAD	268	5.18	80.1	125	3.13	37.0	0.66	40.4	0.58	0.23	0.16
UST quartz (n=30)											
Min	387	3.97	46.9	77.2	2.95	17.1	2.01	107	2.23	0.44	0.11
Max	1487	54.7	477	638	26.9	2017	8.40	421	8.43	8.88	2.72
Median	949	16.3	304	374	10.1	50.0	3.14	169	3.63	1.78	0.49
MAD	240	3.87	79.0	134	2.51	27.1	0.57	36.4	0.81	1.12	0.28
BQ1 (n=20)											
Min	350	6.04	122	49.6	5.19	91.0	1.94	128	2.28	0.36	0.19
Max	1593	50.5	406	2339	15.2	1982	13.6	386	7.59	9.59	1.86
Median	854	17.4	218	333	7.89	637	3.19	191	3.77	1.27	0.48
MAD	126	8.65	25.2	126	1.90	373	0.87	35.2	0.59	0.45	0.20
BQ2 (n=20)											
Min	600	8.57	174	62.3	3.09	45.9	1.95	110	3.11	0.91	0.41
Max	9138	35.6	449	673	21.5	13523	24.3	1505	13.3	13.5	5.28
Median	1132	22.7	292	183	8.39	678	4.51	268	5.08	3.10	1.03
MAD	172	7.16	67.8	76.5	2.85	279	0.97	73.3	0.76	1.45	0.48
BQ3 (n=20)											
Min	304	7.18	108	21.1	2.22	100	1.78	106	2.30	0.35	0.14
Max	1922	26.0	355	665	11.6	1207	65.7	3631	8.18	3.77	15.2
Median	526	13.1	174	73.6	4.70	443	3.55	214	4.27	0.64	0.37
MAD	82.1	3.59	29.2	32.5	1.08	219	1.52	77.3	1.45	0.18	0.13
CQ (n=10)											
Min	1537	58.8	1.33	145	2.25	5.68	2.52	141	2.41	1.03	1.62
Max	6985	201	22.8	1775	6.64	1975	26.8	751	12.7	16.0	27.0
Median	2888	146	8.54	270	3.96	446	5.72	289	3.65	1.95	13.2
MAD	641	26.2	6.45	49.4	0.45	355	2.61	132	1.24	0.34	10.8

Abbreviations: MAD = median absolute deviation, BQ = gray banded vein quartz, CQ = calcite-quartz vein quartz.

1020

Figure 1

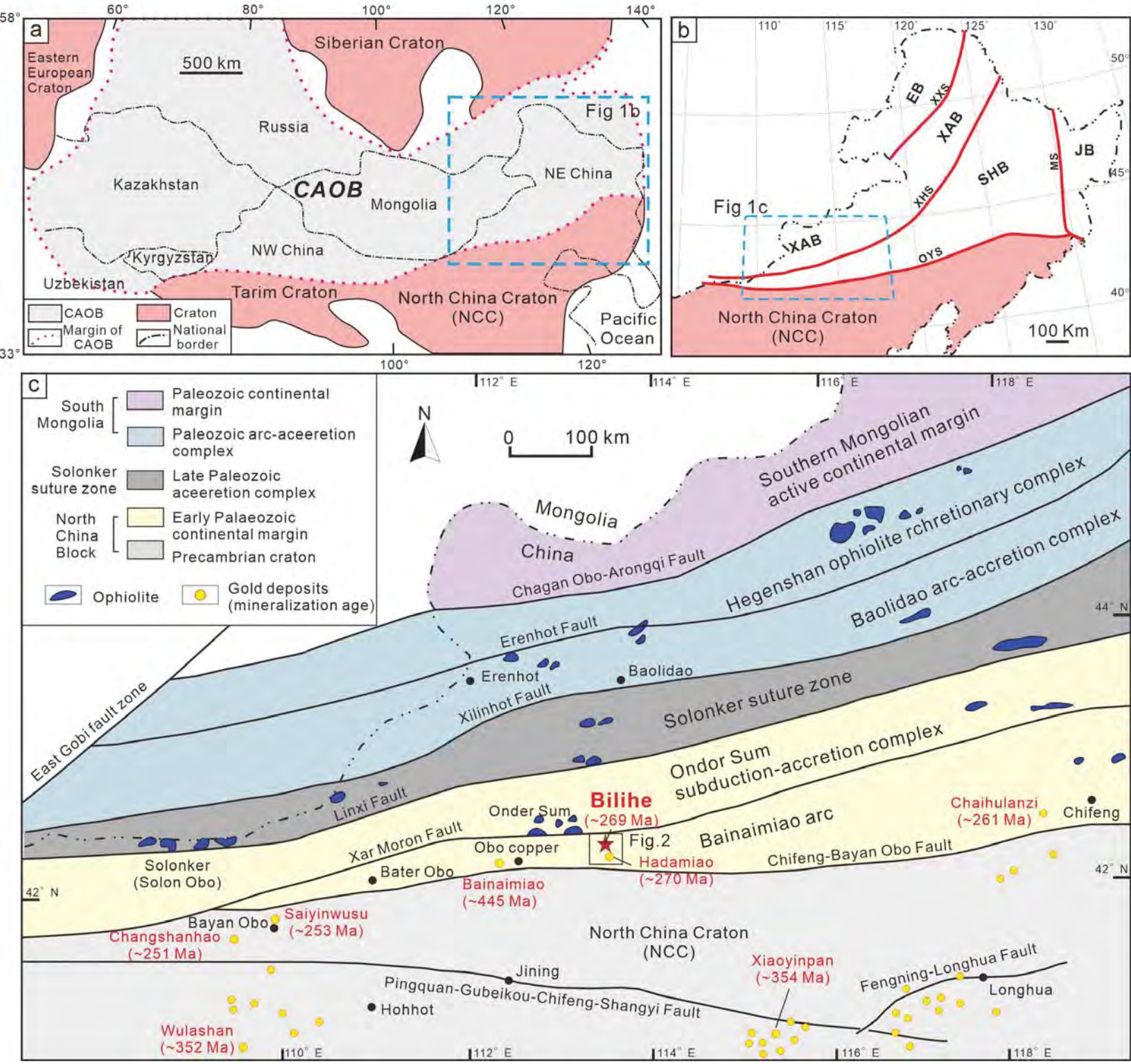

Figure 2

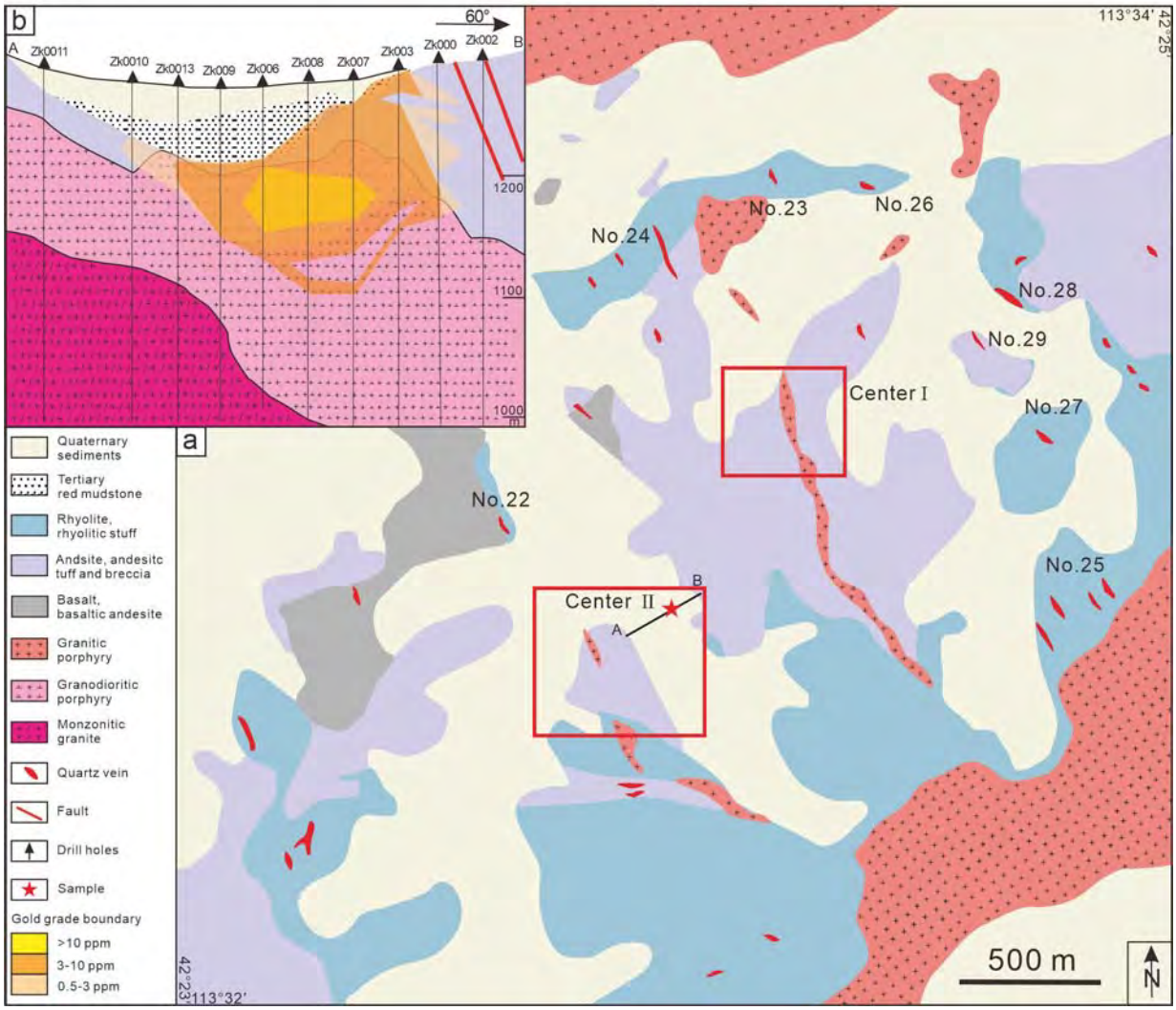

Figure 3

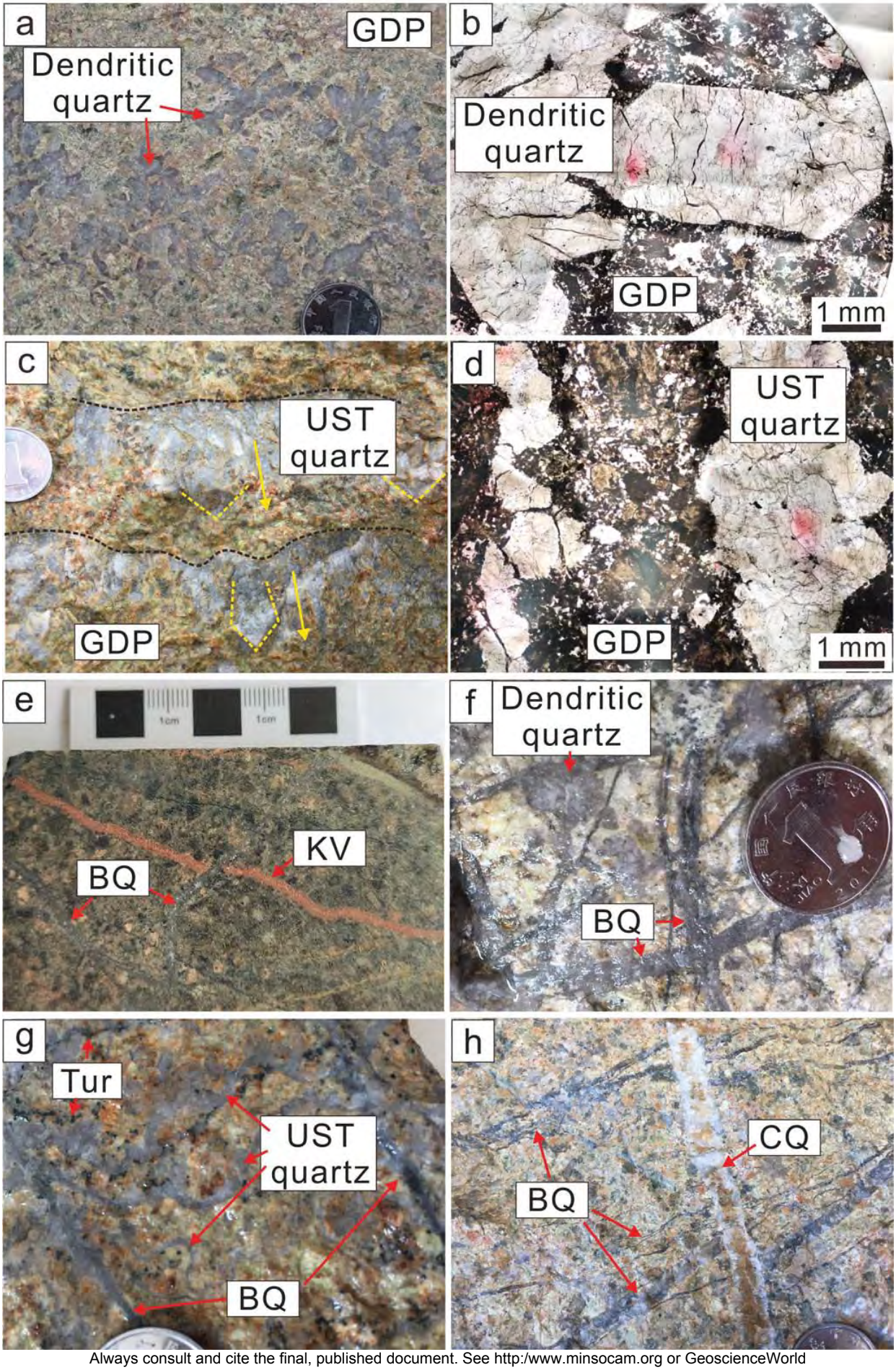

This is the peer-reviewed, final accepted version for American Mineralogist, published by the Mineralogical Society of America.
The published version is subject to change. Cite as Authors (Year) Title. American Mineralogist, in press.
DOI: https://doi.org/10.2138/am-2022-8840. http://www.minsocam.org/

Figure 4

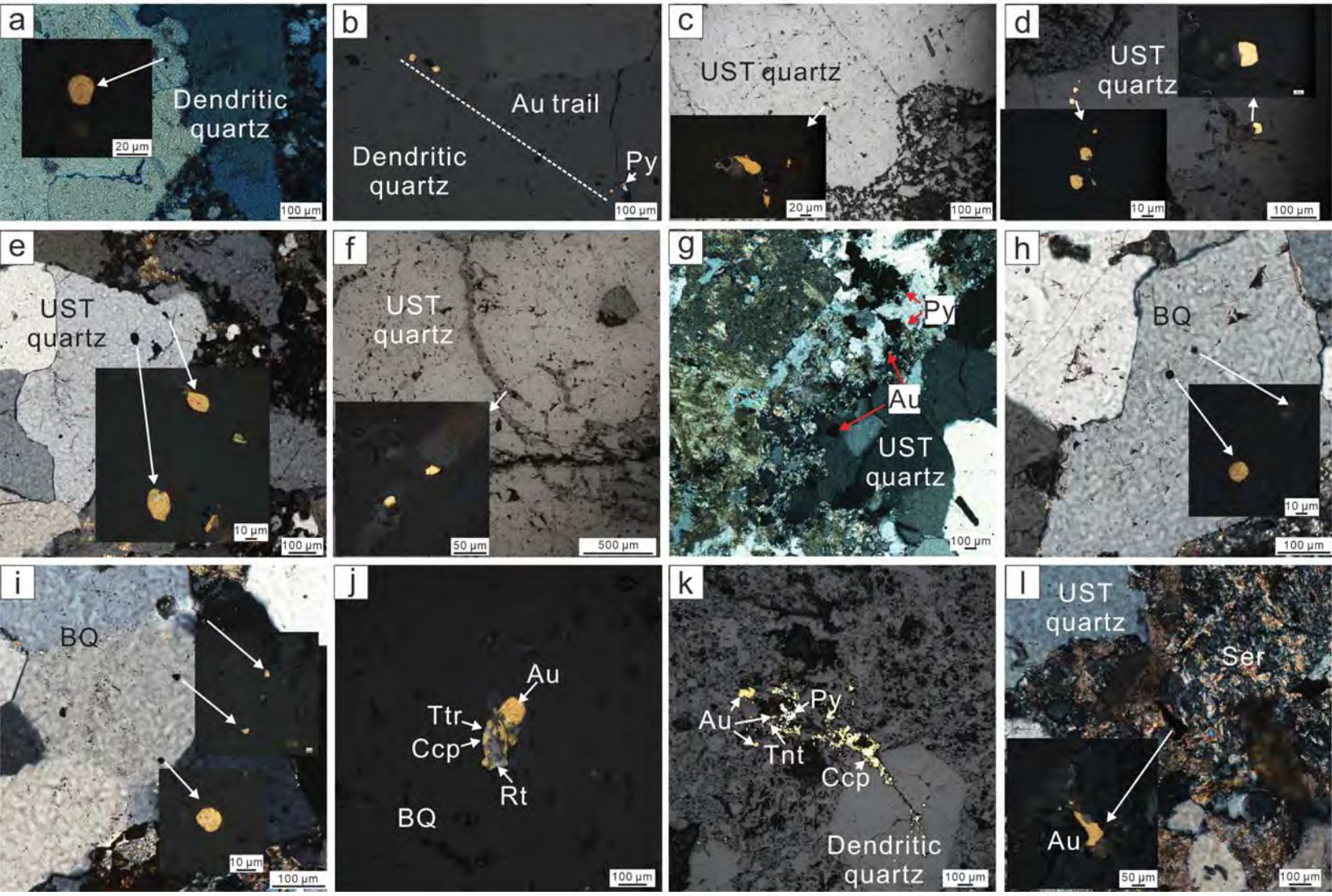

This is the peer-reviewed, final accepted version for American Mineralogist, published by the Mineralogical Society of America.
The published version is subject to change. Cite as Authors (Year) Title. American Mineralogist, in press.
DOI: https://doi.org/10.2138/am-2022-8840. http://www.minsocam.org/

Figure 5

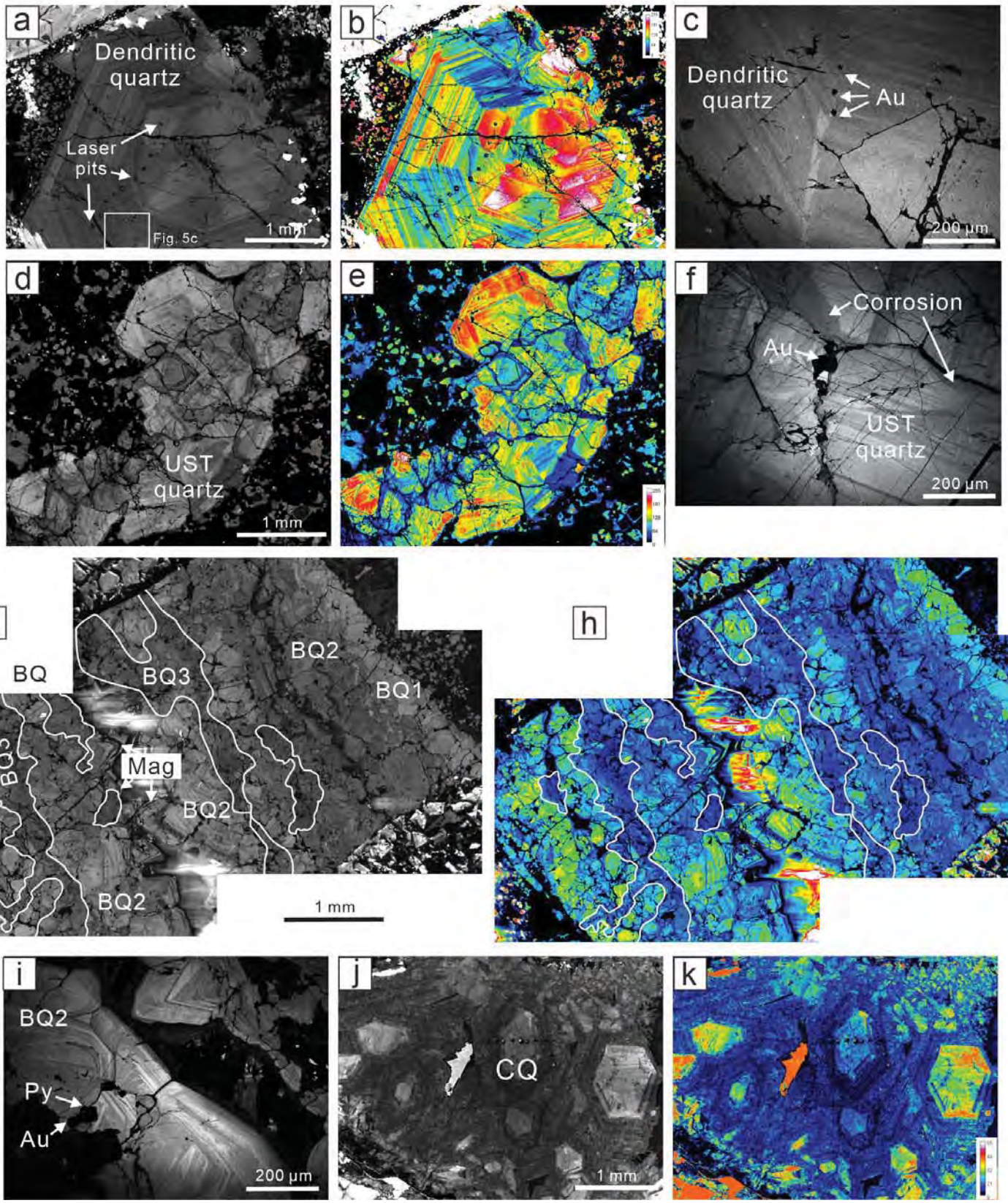

This is the peer-reviewed, final accepted version for American Mineralogist, published by the Mineralogical Society of America.
The published version is subject to change. Cite as Authors (Year) Title. American Mineralogist, in press.
DOI: https://doi.org/10.2138/am-2022-8840. http://www.minsocam.org/

Figure 6

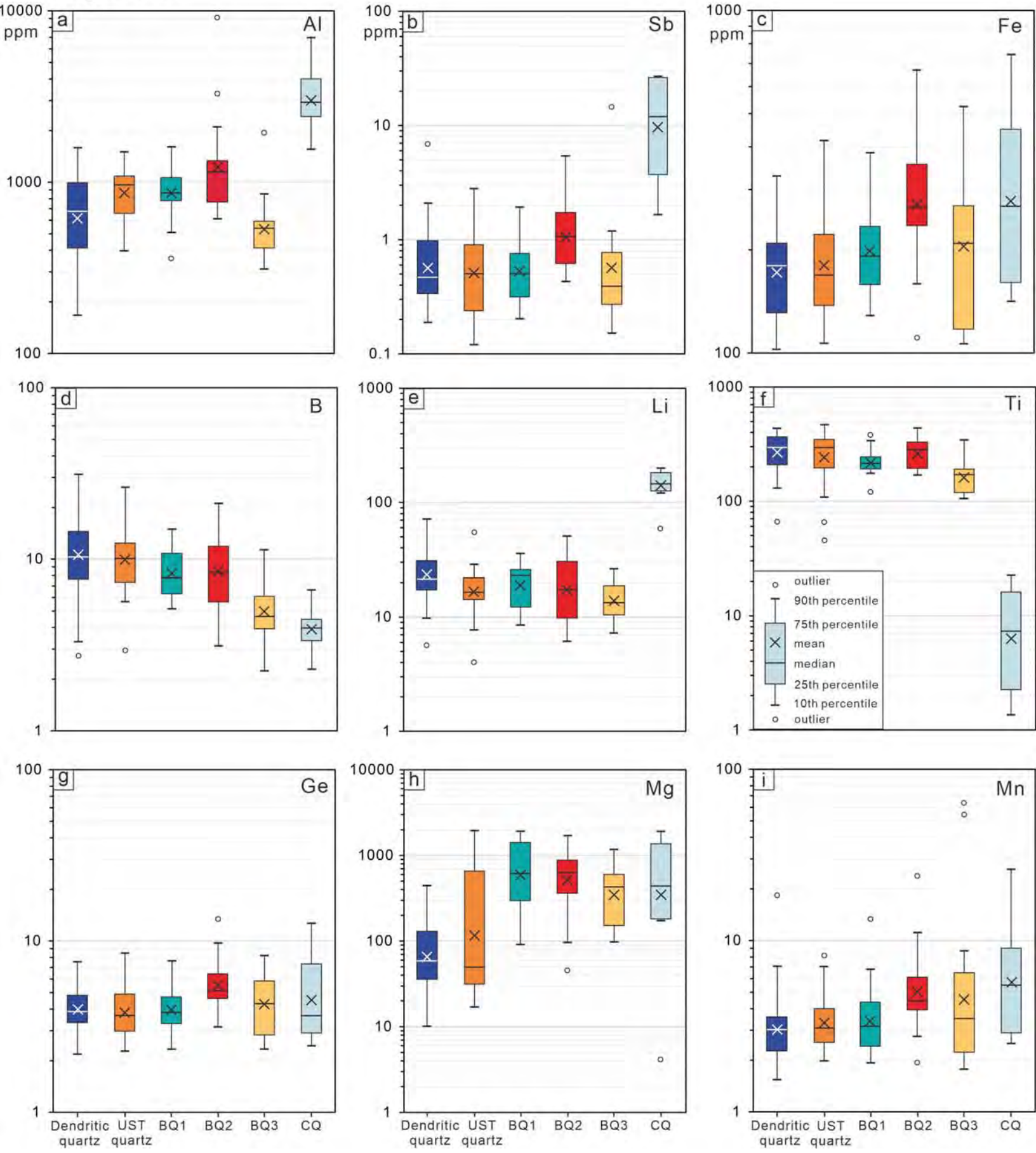

This is the peer-reviewed, final accepted version for American Mineralogist, published by the Mineralogical Society of America.
The published version is subject to change. Cite as Authors (Year) Title. American Mineralogist, in press.
DOI: https://doi.org/10.2138/am-2022-8840. http://www.minsocam.org/

Figure 7

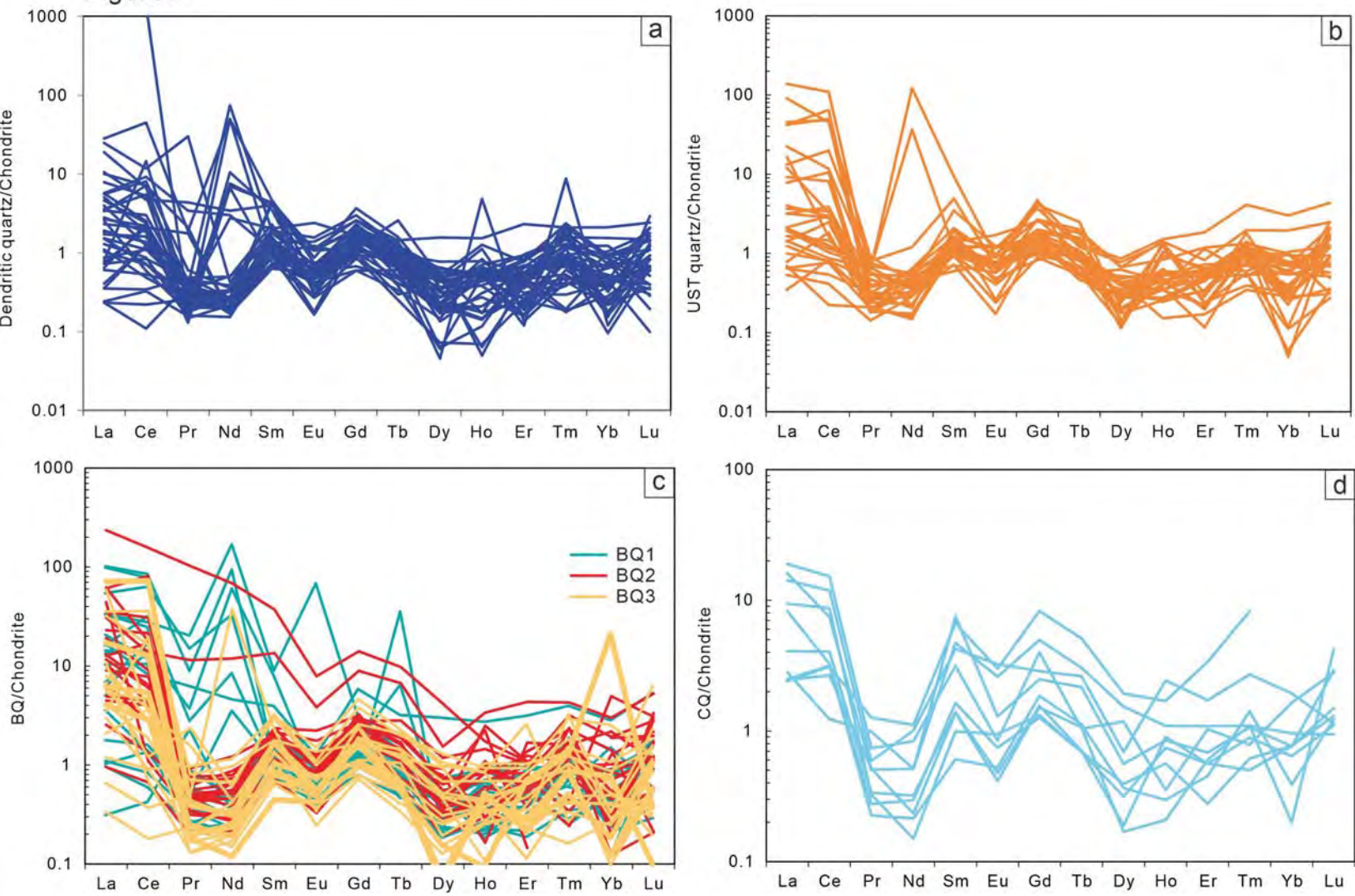

This is the peer-reviewed, final accepted version for American Mineralogist, published by the Mineralogical Society of America.
The published version is subject to change. Cite as Authors (Year) Title. American Mineralogist, in press.
DOI: https://doi.org/10.2138/am-2022-8840. http://www.minsocam.org/

Figure 8

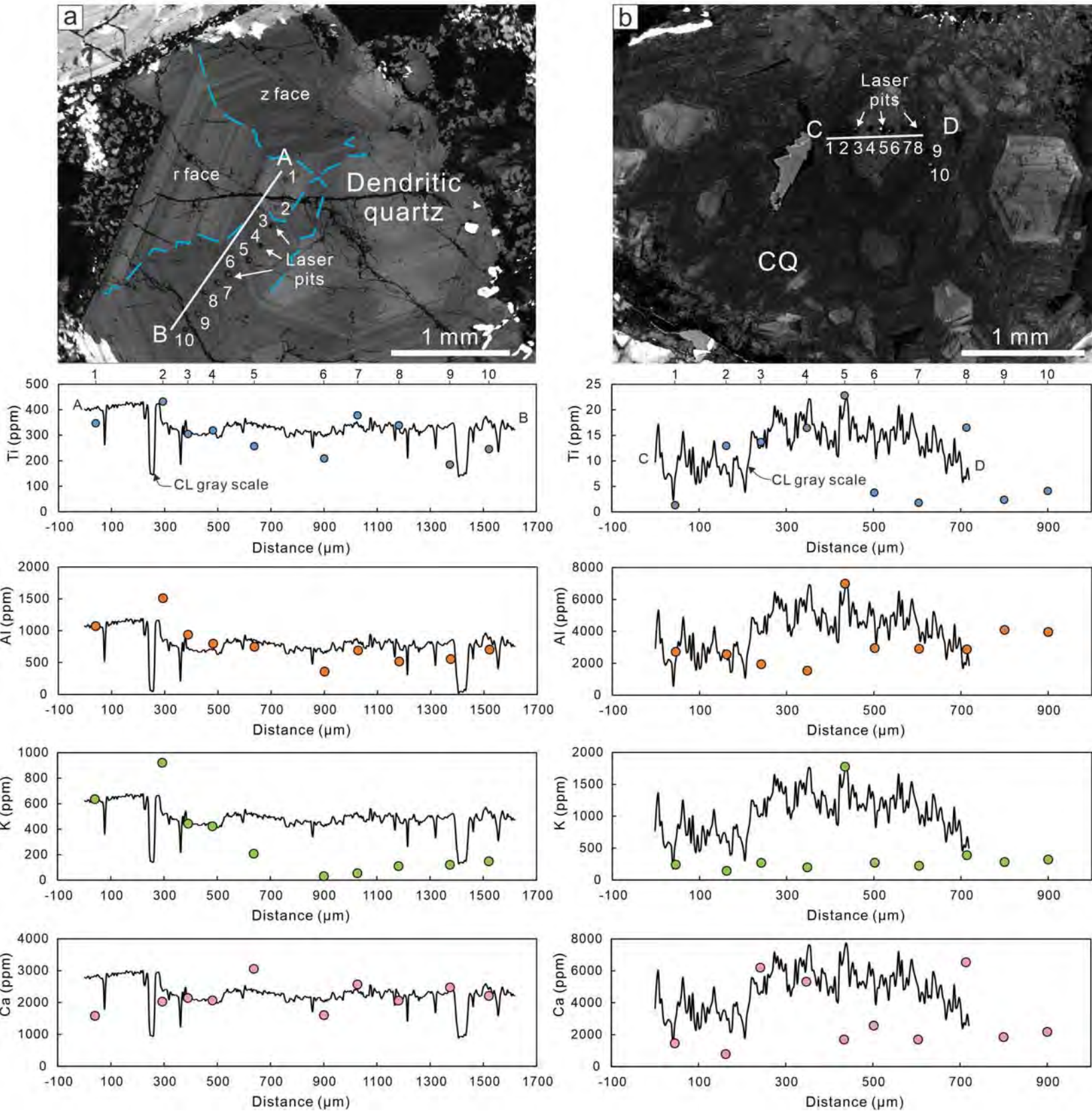

This is the peer-reviewed, final accepted version for American Mineralogist, published by the Mineralogical Society of America.
The published version is subject to change. Cite as Authors (Year) Title. American Mineralogist, in press.
DOI: https://doi.org/10.2138/am-2022-8840. http://www.minsocam.org/

Figure 9

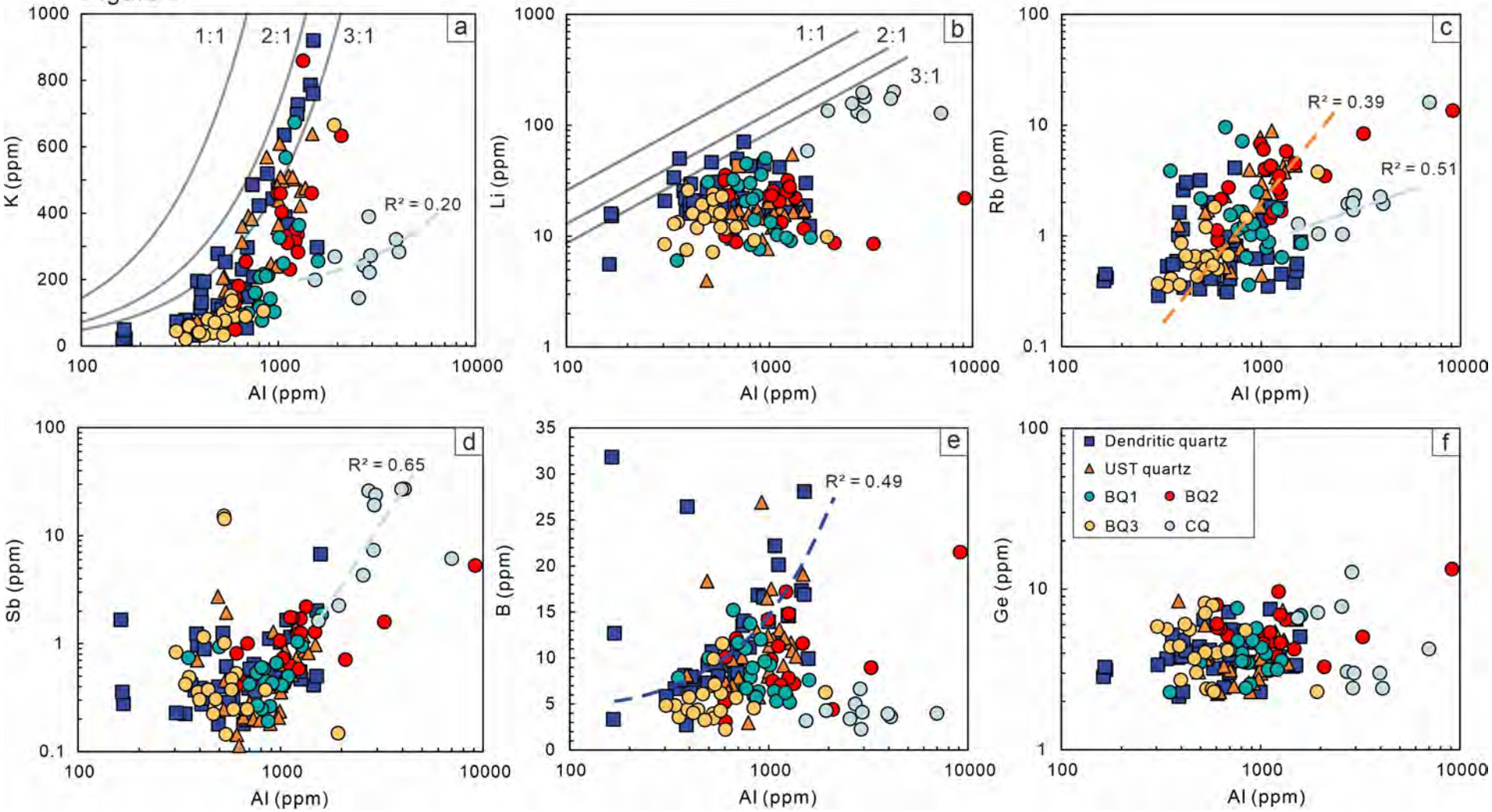

This is the peer-reviewed, final accepted version for American Mineralogist, published by the Mineralogical Society of America.
The published version is subject to change. Cite as Authors (Year) Title. American Mineralogist, in press.
DOI: https://doi.org/10.2138/am-2022-8840. http://www.minsocam.org/

Figure 10

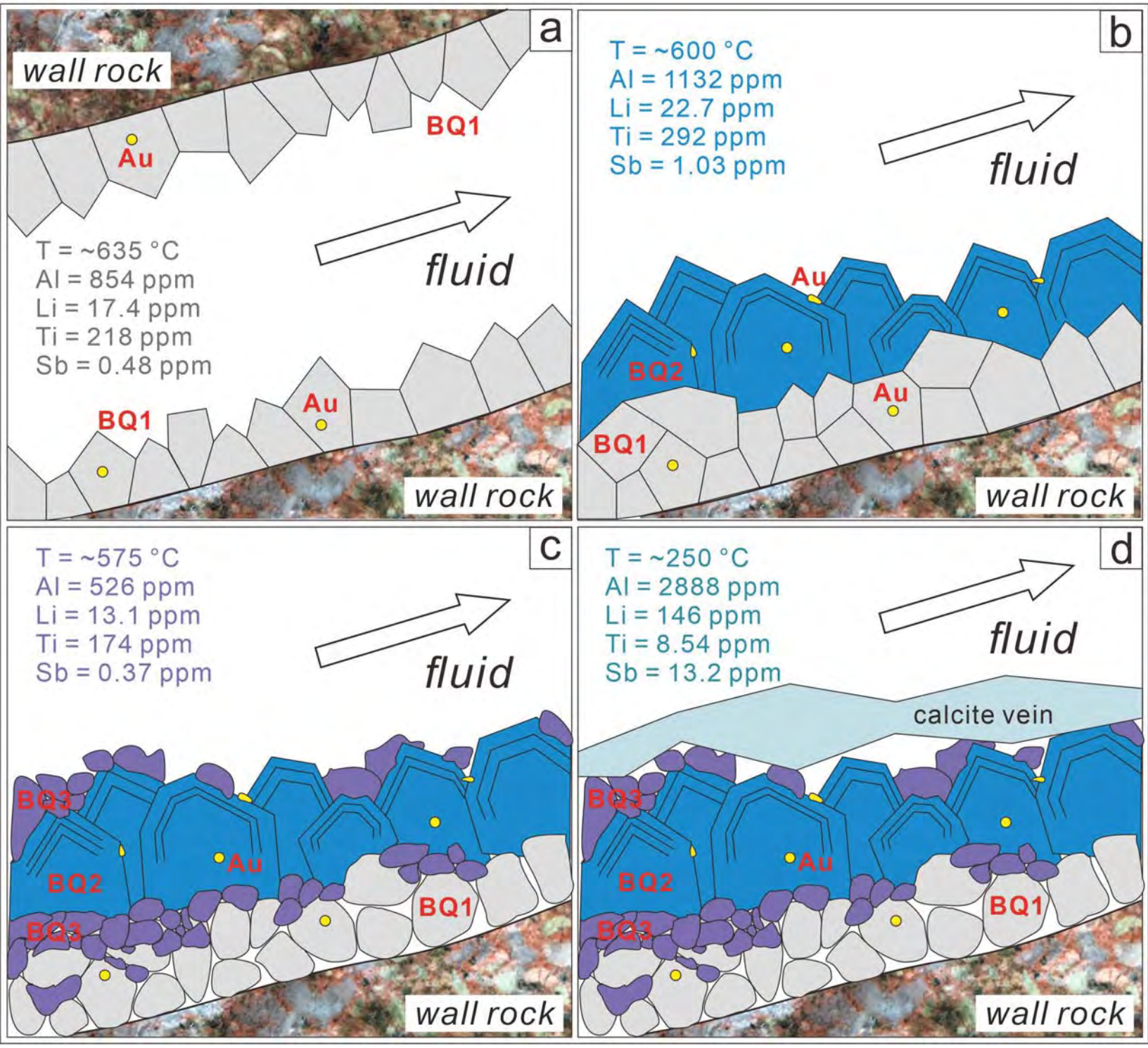

Figure 11